CZECH TECHNICAL UNIVERSITY IN PRAGUE

Faculty of Nuclear Sciences and Physical Engineering

Department of Physics

Research project

Production of non-photonic electron in STAR experiment

Bc. Katarína Gajdošová

Supervisor: Mgr. Jaroslav Bielčík, Ph.D.

Consultant: Ing. Olga Rusňáková

Prague, 2014

Prehlásenie

Prehlasujem, že som svoju výskumnú úlohu vypracovala samostatne a použila som len literatúru a publikácie uvedené v priloženom zozname.

Nemám závažný dôvod proti použitiu tohoto školského diela v zmysle §60 Zákona č.121/1200Sb., o autorskom práve, o právach súvisiacich s autorským právom a o zmene niektorých zákonov (autorský zákon).

V Prahe dňa ....

Acknowledgements

I would like to give thanks to my supervisor, Mgr. Jaroslav Bielčík Ph.D., for his support and intereset in my work, to my konsultant Ing. Olga Rusňáková and finally to Mustafa Mustafa, Ph.D. for his patience and unvaluable help and discussions.

Názov práce: **Produkcia nefotonických elektrónov v experimente STAR**
Autor: Katarína Gajdošová

Odbor: Jadrové inžinierstvo
Druh pr Výskumná úloha

Veduci prace: Mgr. Jaroslav Bielčík, Ph.D.
Katedra fyziky, Fakulta jaderná a fyzikálne inženýrská,
České vysoké učení technické v Praze.

Abstrakt:

Kvark-gluónová plazma je stav veľmi hustej a horúcej jadrovej hmoty. Kvarky a gluóny sa tu vyskytujú v neviazanom stave. Tento stav hmoty sme schopní vytvoriť pri zrážaní dvoch jadier pri vysokých energiách. Najznámejšie experimenty, ktoré sa zaoberajú kvark-gluónovou plazmou, sú ALICE na Veľkom hadrónovom urýchľovači LHC, a STAR na Relativistickom urýchľovači ťažkých jadier RHIC. QGP je možné študovať len nepriamo porovnávaním vlastností vzniknutých častíc v zrážkach s prítomnosťou QGP a bez nej. V tejto práci sa budem hlavne zaoberať štúdiom otvorených ťažkých vôní, medzi ktoré patrí aj meranie nefotonických elektrónov.

Klúčové slová: kvark-gluónová plazma, STAR, nefotonické elektróny

Title: **Production of non-photonic electrons in STAR experiment**
Author: Katarína Gajdošová

Abstract:

Quark-gluon plasma is a state of very hot and dense nuclear matter. Quarks and gluons exist here in unbounded state. We are able to create this phase of matter by colliding two heavy ions at very high energies. The well-known experiments that explore the quark-gluon plasma, are ALICE at Large Hadron Collider, LHC, and STAR at Relativistic Heavy Ion Collider, RHIC. We can study the QGP only indirectly by comparing the properties of originated particles in collisions with presence of QGP and without QGP. In this work I will describe mainly the study of open heavy flavor, among which also belongs the measurement of non-photonic electrons.

Keywords: quark-gluon plasma, STAR, non-photonic electrons

Contents

List of Figures

List of Tables

Introduction

One of the main research programms of these days is the study of hot and dense matter called quark-gluon plasma (QGP). It is a state of deconfined quarks and gluons where these can move almost as free particles. We suppose that QGP was created at the beginning of the universe. If we want to study this state of matter we must create the same conditions as were at the Big Bang. In order to do this, the Relativistic Heavy Ion Collider in Brookhaven National Laboratory collides heavy nuclei such as gold or uranium at ultra-relativistic energies.

In this thesis I will focus on heavy flavor physics that investigate what happens to heavy quarks as c and b quark during the collision. These quarks are created at the beginning of the collision in hard processes so they are influenced by all following stages of the collision. Study of open heavy flavor is one of the possibilities to trace back how does the QGP look like. This is topic of the first chapter.

In the second chapter I will describe the STAR detector, which is important for detecting particles coming from the collision. The subsystems that are needed for my analysis are Time Projection Chamber TPC, Time of Flight TOF, Barrel Electromagnetic Calorimeter BEMC and finally newely installer Muon Telescope Detector MTD. Brief description of composition and funcionality of these detectors is mentioned.

Third chapter is dedicated to description of the mechanism of analysis of non-photonic electrons. These electrons come from semileptonic decays of D or B mesons, so they are good probes for the study of QGP. I also presented latest results of nuclear modification factor of NPE. The suppression is much larger than we expected, but for more precise statements we have to wait for data with more statistics.

In the last chapter I will present my analysis of non-photonic electrons in UU collisions at energy $\sqrt{s} = 193$ GeV in STAR experiment. I will describe all steps that I have worked on during the first year of Master studies in detail.

Chapter 1

Heavy flavor physics in STAR experiment

1.1 Introduction to quark-gluon plasma

The main purpose of the STAR experiment is to investigate a hot and dense medium called the quark-gluon plasma. The main building blocks of nature, quarks and gluons, are in deconfined state in this medium. We still don't know how to properly describe the QGP. Perturbative quantum chromodynamics works well for matter created in proton-proton collisions, that is not the QGP, but it fails at description of medium created in heavy-ion collisions.

Nowadays we are able to create the quark-gluon plasma in heavy-ion collisions at high energies. Such collisions take place in synchrotron accelerators, where beams of heavy ions such as nuclei of gold or lead circulate in two independent beam pipes in opposite directions, and at the point where a detector is located the beam pipes intersect and heavy ions collide. These particles are accelerated at almost the speed of light, so as a consecuence of Lorentz contraction along the direction of their movement they squeeze and form the so called "pancakes". At the moment of a collision, these pancakes pass through each other and as they are drawning apart a "fire-ball" is created, where is a great probability of formation of QGP. The created system is expanding during first fs after the collision mainly in longitudinal direction because nuclei are receeding with almost the speed of light.

The phase diagram of transition between quark-gluon plasma and hadron gas is still object of intense research. On the Figure 1.1 the phase transition diagram is shown in terms of tepmerature of the system T and baryo-chemical potential μ_b. The quark-gluon plasma phase exists below the transition line, which represents the first order phase transition. For low baryo-chemical potentials and high temperatures the so called rapid cross-over takes place. Modern accelerating facilities, for example LHC in CERN or RHIC in BNL, can reach points of this diagram that lies at the cross-over region or even higher. For low μ_b the critical temperature of phase transition is estimated to be $T_{crit} = 175$ MeV [4].

Right after the collision of heavy ions at sufficient center of mass energy, the quark-gluon plasma can be created. We can divide the evolution of the created system into various stages. The diagram on Figure 1.2 illustrates different moments of the collision that are described below. As was mentioned before, the created system is expanding mainly in longitudinal direction that allows us to describe the space-time evolution of the collision in terms of time t and direction of the incoming beam of particles z. The proper

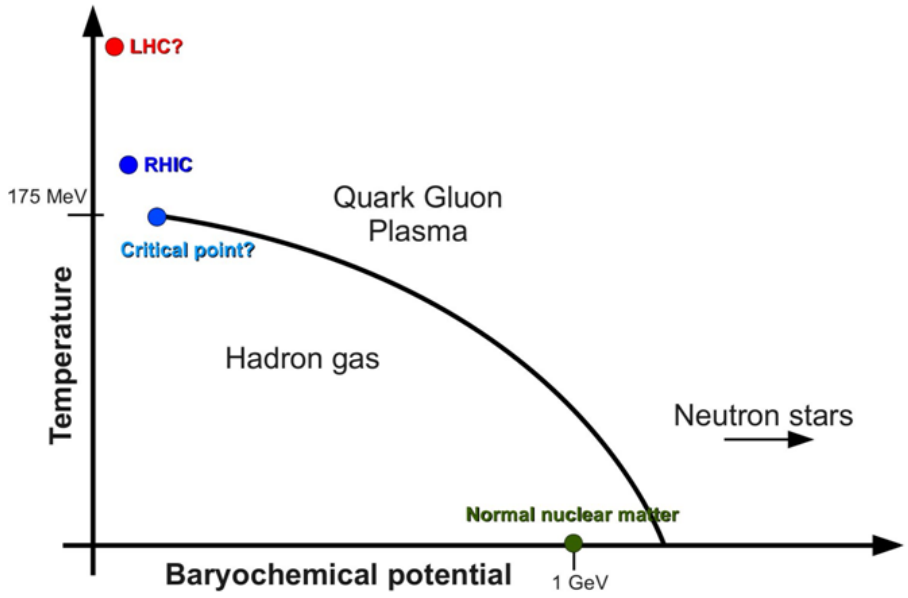

Figure 1.1: The phase diagram showing the phase transition between quark-gluon plasma and hadron gas. For low μ_b and temperature $\sim$ 175 MeV a cross-over takes place, from critical point towards higher μ_b there is a first order phase transition. Taken from [7].

time τ is situated on hyperbolas of the diagram.

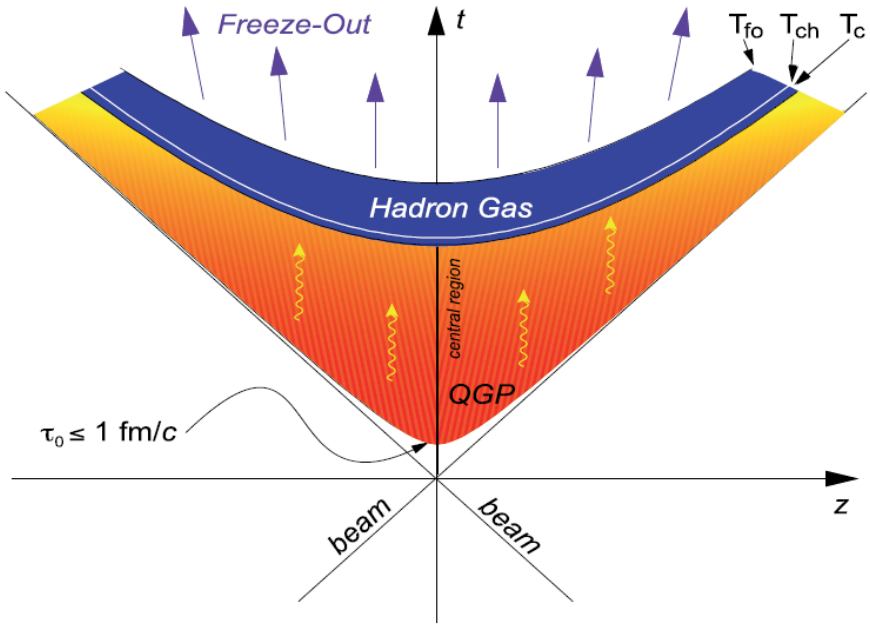

Figure 1.2: The space-time diagram of different stages of a heavy-ion collision. At proper time τ_0 the system comes to thermal equilibrium and QGP is present. At T_c the phase transition to hadron gas takes place. T_{ch} is the temperature of chemical freeze-out and T_{fo} temperature of kinetic freeze-out. Taken from [4].

We can divide the evolution of the system after the collision in the following stages [4]:

- Right after the collision of the nuclei the system is composed of excited virtual quanta and it will take time to deexcite and form quarks and gluons. Heavy quarks can be created in hard scatterings with large transported momentum. The system is in the pre-equilibrium phase.
- At proper time $\tau_0 \approx 1$ fm/c the system comes to thermal equilibrium and quark-gluon plasma is created. This stage of the collision is well described by hydrodynamics.
- At critical temperature $T_c \approx 175$ MeV the system undergoes a phase transition from QGP to hadron phase, quarks and gluons are no longer free but connected by the strong force into hadrons.
- At high baryo-chemical potential we can distinguish between two types of freeze-out. At $\tau_{ch} < \tau_{fo}$ there is a chemical freeze-out after which particles no longer suffer inelastic scatterings, but they can still lose their energy by elastic collisions with other particles of the system. The ratio of different particle species remains constant. At τ_{fo} the kinematic freeze-out takes place. At this point elastic collisions cease, particles do not lose their energy and fly away into the vacuum. For low values of baryo-chemical potential these two freeze-outs occur at same proper time.

1.2 Clasification of heavy-ion collisions

Particle accelerators can collide various heavy ions, for example gold, lead or uranium. Both have very big atomic numbers, so if they collide, many nucleon-nucleon collisions occur. Collisions where all nucleons participate, the so called central collisions, do not happen all the time. It is clear that the more nucleons participating in collision, the bigger is the probability of formation of QGP. Therefore we need to clasify collisions according to their centrality.

Centrality of the collision is defined with the impact parameter b that is the distance between centers of colliding nuclei. When $b = 0$ the collision is central, for $0 < b < 2R$ we call the collisions periferal, and for $b > 2R$ ultraperipheral. On the Figure 1.3 there is an illustration of different types of centrality of heavy-ion collisions.

However, we are not able to measure the impact parameter b. One way in which we can define the centrality is through Glauber model. This model assumes a nucleus-nucleus collision as a multiple nucleon-nucleon collisions. The nucleon-nucleon collision is characterized by total inelastic cross section σ_{ine}.

We can divide the multiplicity distribution i.e., the number of particles produced, into various bins of centrality and then correlate them through the model with impact parameter and number of participants. A participant is a nucleon that undergoes at least one inelastic collision. In the Figure 1.4 can be seen the multiplicity distribution cut into centrality bins, where the maximum values of charged particles corresponds to top 5 % central collisions. On the upper side of the figure there are axes labeled as N_{part} and b that are assigned to this plot by Glauber model.

1.3 Heavy flavor physics

Quark-gluon plasma is the main field of study of the STAR experiment. Unfortunately, it exists only for few fs after the collision and we are not able to study it directly. Heavy flavor quarks are created during the first stages of heavy-ion collisions in hard processes, when partons transfer large amount of momentum between themselfs. These quarks are then

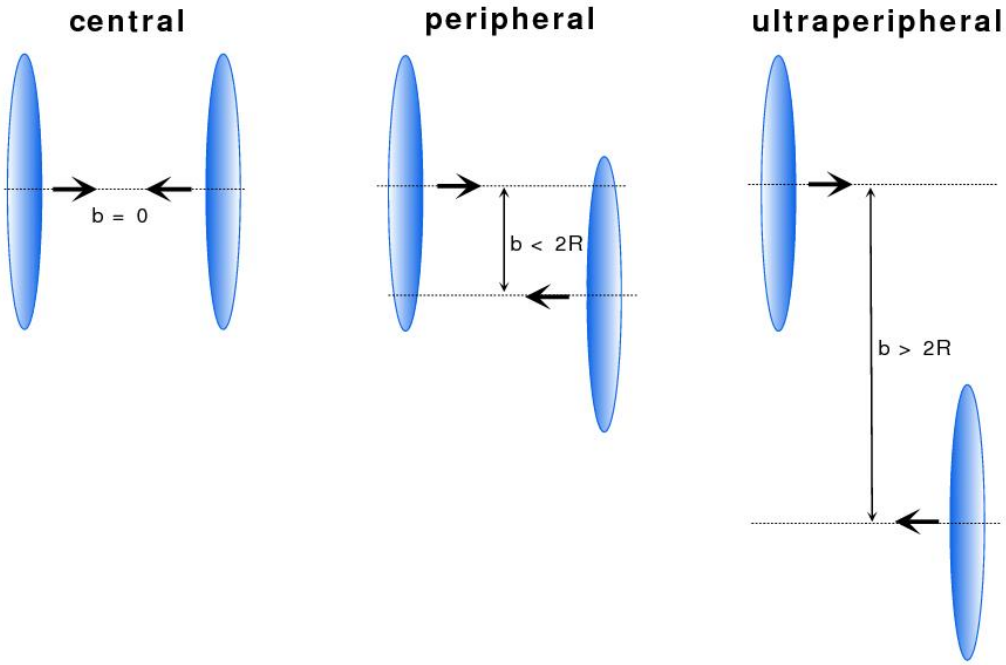

Figure 1.3: Illustration of different types of centrality of a collision of heavy nuclei. From left to right: central, peripheral and ultraperipheral collisions.

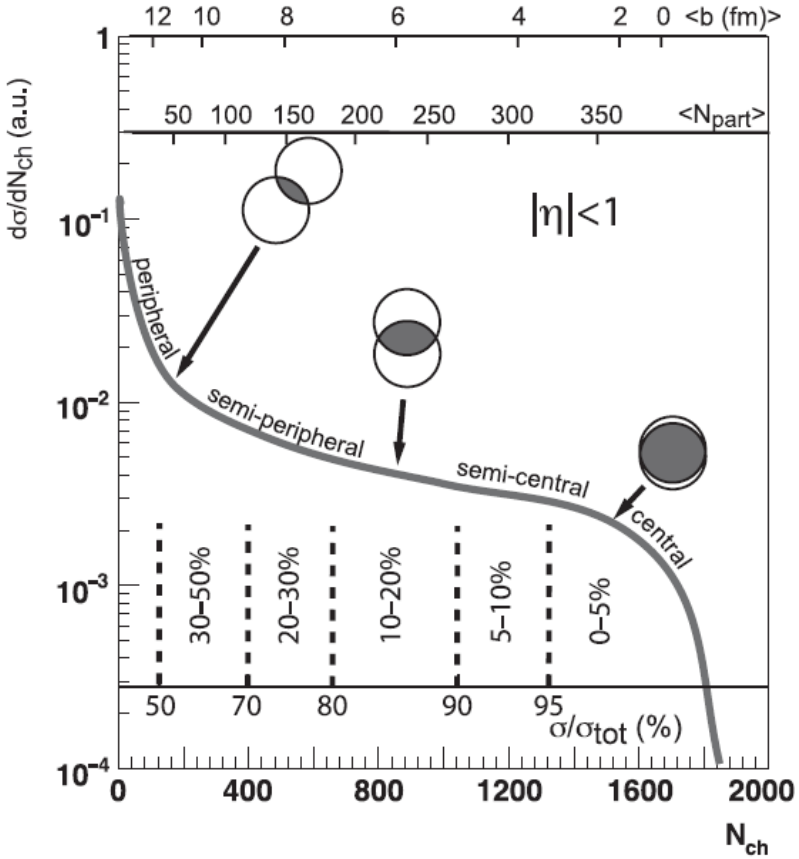

Figure 1.4: Multiplicity distribution with assigned bins of centrality through Glabuer model to impact parameter and number of charged particles that participated in collision. Taken from [6].

present during all following stages of the collision. They are affected by the interactions with fields and forces in quark-gluon plasma and so are particles formed of heavy quarks created during last stages of the collision. Heavy flavor particles composed of heavy quarks are therefore appropriate probes that help us to look back at what happened in QGP. First I will present here some useful observables and processes that occur in QGP.

1.3.1 Nuclear modification factor

As we cannot study the quark-gluon plasma directly, we must rely on the properties of the particles coming out to our detectors after the freeze-out. If we want to know the effects of QGP on particle production, we have to compare this production to a system in which no QGP is formed. Such a system is a proton-proton collision.

An observable suitable for studying the effects of QGP on particle production is nuclear modification factor R_{AB} defined as ratio of particle production in heavy-ion collisions to proton-proton collisions. To get relevant information, we must compare the productions always at the same conditions, that is the energy, centrality (impact parameter), transverse momentum p_T and rapidity η. The ratio is scaled by nuclear overlap function $\langle T_{AB}\rangle(b)$ from Glauber model that represents number of nucleon-nucleon collisions in a single nucleus-nucleus collision at given impact parameter [4].

$$R_{AB}(p_T, y, b) = \frac{d^2N_{AB}/dydp_T}{\langle T_{AB}\rangle(b)d^2\sigma_{pp}/dydp_T} \tag{1.1}$$

We expect that in QGP quarks and gluons suffer some energy loss by interactions with the strongly interacting medium. Therefore for example particles at pp collisions that are observed with high p_T will not be detected at the same p_T bin when coming from heavy-ion collisions. These particles would loose some energy in QGP and will be observed with low p_T. Thus, comparing the particle production from heavy-ion collisions to proton-proton collisions at high p_T we should see less particle production. Also due to color screening some particles that would have been formed are decomposed and we cannot observe them which causes a particle production suppression too. More about this phenomena will be discussed below.

If the R_{AB} is equal to one, that means no QGP is formed and heavy ion collisions are just a superposition of nucleon-nucleon (proton-proton) collisions. If $R_{AB} > 1$ we call it an enhancement which can be caused by Cronin effect. It can be seen in assymetric collisions, for expample deuteron-gold, where no QGP is formed, but multiple scatterings are present which leads to higher number of particles with low momentum than in pp collisions. Finally, if $R_{AB} < 1$, we are talking about suppression. Particles lose energy or are melted in QGP, so the final production is smaller than the production from pp collisions. I illustrate this situation on Figure 1.5. In d-Au collisions we can see a Cronin effect and in Au-Au collisions a strong suppression is present.

If we do not have the reference data from pp collisions, we can use other form of nuclear modification factor, R_{CP}, defined as ratio of production of particles in central collisions with respect to peripheral collisions. As it was said, in central collisions the existence of QGP is more probable, so we should see some suppression. The bigger the centrality is in numerator and smaller in denominator, the bigger the factor of suppression is. The fraction is again scaled by overlap functions from Glauber model.

$$R_{CP}(p_T, y,) = \frac{d^2N_h(b_1)/dydp_T}{d^2N_h(b_2)/dydp_T}\frac{\langle T_{AB}\rangle(b_2)}{\langle T_{AB}\rangle(b_1)} \tag{1.2}$$

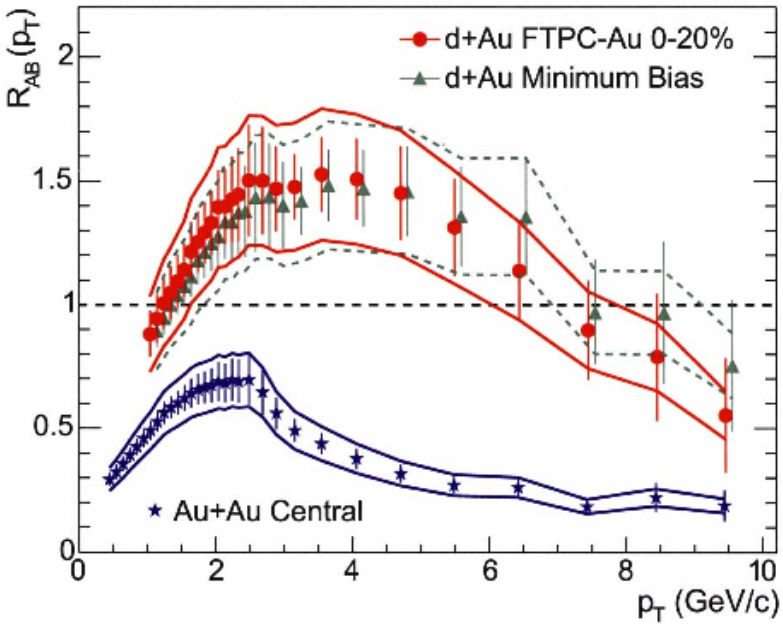

Figure 1.5: Nuclear modification factor of charged hadrons in dAu and AuAu collisions from STAR experiment. In dAu collisions a Cronin effect can be seen and in heavy-ion collisions a suppression is observed. Taken from [10].

1.3.2 Jet quenching

As was mentioned before, the quark-gluon plasma cannot be observed directly. We have to rely on appropriate probes that can reveal us some consecuences of interaction of particles with this kind of matter. One of these useful probes is jet quenching.

Two energetic partons are created in hard processes with large transferred momentum. In case they are created close to the surface of the fireball, one of them flies out of this medium and the second one goes in the opposite direction through the medium. As the parton passes through QGP, it can lose energy by interactions with strongly interacting medium. Experimentally we observe a jet of particles created from fragmentation of the parton. A scheme of this process can be seen on the Figure 1.6. On the left picture there is a proton-proton collision, where no QGP is created. As two quarks collide in a hard process, two partons originate in opposite directions forming a jet of particles as they are flying away. There is no medium that could cause strong interactions, so there are two fully evolved jets in both directions. On the other side, on the right picture there is a nucleus-nucleus collision where a QGP is formed. In hard process two partons are created near the surface of the fireball from which one propagates through the medium and flies quenched out, and the second jet is almost unquenched.

When we study azimuthal distribution of hadrons with high p_T in heavy-ion collisions, we should see that associated opposite jets are quenched after passing through QGP. An example of this distribution is shown on Figure 1.7. We select a hadron with transverse momentum $p_T \geq 4$ GeV/c in azimuth angle φ_{trigg} and we study the distribution of hadrons with $p_T \geq 2$ GeV/c dependent on $\Delta\varphi = \varphi - \varphi_{trigg}$. We define as "near-side" azimuthal domain around angle φ_{trigg} and as "away-side" the opposite domain around $\Delta\varphi \approx \pi$, where in case of no QGP formed we can find the associated opposite jet. On the Figure 1.7 we can see a clear opposite signal in pp and dAu collisions, while in AuAu collisions the opposite jet totally disappears. We interpret this as a consecuence of energy loss of opposite parton passing through strongly interacting medium [4].

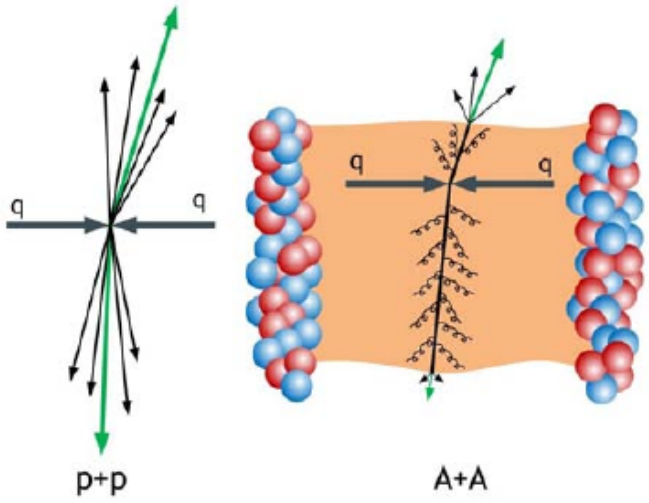

Figure 1.6: Jet quenching - a scheme of a pp and AA collision. In pp collisions there is no QGP, outgoing particles are not quenched by the interaction with QGP. In AA collisions a strongly interacting medium is created and as a consecuence the production of particles with high p_T is suppressed. Taken from [12].

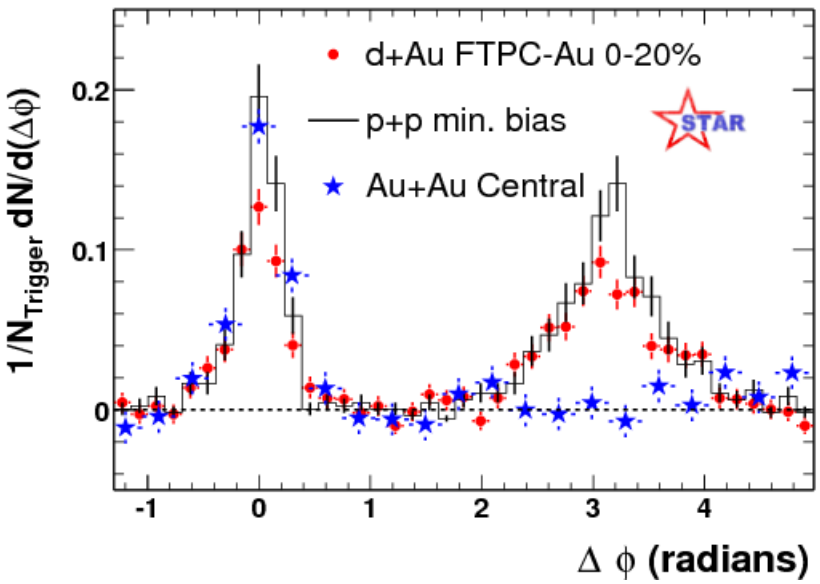

Figure 1.7: Azimuthal di-hadron correlation from di-jet production in STAR at energy $\sqrt{s_{NN}} = 200$ GeV. Trigger particle with $p_T \geq 4$ GeV/c is at angle $\Phi = 0$, "away-side" signal measured for particles with $p_T \geq 2$ GeV/c is at angle $\Delta\Phi = \pi$. Taken from [4].

As a consequence of jet quenching we observe a suppression of production of particles with high transverse momentum ($p_T \gtrsim 2$ GeV/c). High-energetic partons lose their energy via interactions with the QGP before they can hadronize, so they lose some of their transverse momentum. Particles formed of these partons also have smaller values of p_T. Thus they no more belong to a group of particles with high transverse momenta which leads to suppression of these particles in comparison with system where no QGP is present. This behaviour should be seen in terms of nuclear modification factor R_{AA}. It is defined according the formula 1.1 as ratio of particle production in heavy-ion collisions to pp collisions. Thus when studying the production of particles with high p_T this ratio should be below 1 that is called suppression.

1.3.3 Dead-cone effect

There are mainly two types of energy loss of quarks in QGP: collisional and radiative. In radiative losses a gluon bremsstrahlung is an important feature. The statement of the dead-cone effect is that for heavy quarks the amount of gluon radiation is smaller then that of light quarks [13].

The radiation of gluons is suppressed at angles smaller than the ratio of its mass and energy $\theta < m/E$. The distribution of gluons with energy ω and transverse momentum $k \approx \omega\theta$ emmited off a heavy quark is suppressed in comparison with standard bremsstrahlung spectrum by a factor

$$\omega \frac{dI_{rad}}{d\omega dk^2}(1 + \frac{\theta_0^2}{\theta^2})^{-2} \tag{1.3}$$

where $\theta_0 = \frac{m}{E}$ [13].

The bigger the mass of a quark is, the bigger is the angle θ_0 and the bigger is the number we divide the distribution with, resulting in suppressed distribution of emitted gluons. Therefore, the bigger the quark mass is, the smaller is the radiation of gluons and the smaller is the energy loss of the quark.

1.4 Why is the study of heavy flavor important

As was mentioned at the beginning of this chapter, heavy quarks are created mainly in hard processes during first stages of a heavy-ion collision which makes them a good probe for the study of QGP. The strongly interacting medium affects the production of particles composed of heavy quarks. Main effects studied in heavy flavor are sequential suppression of quarkonia and suppression of open heavy flavor at high p_T in comparison with suppression of light hadrons composed of light quarks. Each of this effects is described below in separate sections.

1.4.1 Quarkonia

Quarkonia are particles that consist of one heavy quark and antiquark with the same flavor. Particles composed of charm quarks are called charmonia, and hadrons composed of bottom quarks are bottomia. Quarkonia that are at their ground state are strongly coupled e.g., J/ψ for charmonia and Υ(1S) for bottomia. There are other less bounded states of quarkonia in higher states. In the Table 1.1 the basic types of quarkonia are shown.

Because of the shape of the confining potential that is described by relation 1.4 where $\sigma = 0,2$ GeV^2 is the string tension and $\alpha = \pi/12$ is the gauge coupling, quarkonia with

quarkonium	content	mass [MeV/c^2]	quarkonium	content	mass [Mev/c^2]
J/ψ	$c\bar{c}$	3096,92	$\Upsilon(1S)$	$b\bar{b}$	9460,30
χ_c	$c\bar{c}$	3510,66	$\Upsilon(2S)$	$b\bar{b}$	10023,26
ψ'	$c\bar{c}$	3686,11	$\Upsilon(3S)$	$b\bar{b}$	10355,2

Table 1.1: Properties of quarkonia. Taken from [1].

different confining potential have different radius r_c [4].

$$V(r) = \sigma r - \frac{\alpha}{r} \tag{1.4}$$

Quarkonia that are strongly confined, have smaller radius and viceversa. This feature is important because we can use quarkonia as a thermometer of nuclear matter. For temperatures $T > T_c$ the potential of quarkonia changes due to Debeye screening of free color charges as

$$V(r) = -\frac{\alpha}{r} \exp\left[-r/r_D(T)\right], \tag{1.5}$$

where r_D(T) is Debeye screening radius [4]. When the screening radius is smaller than the radius of quarkonia, heavy quarks coupled in pairs cannot see each other because of the color screening. As the tepmerature increases, the Debeye screening radius decreases, and more tightly bounded states melt in QGP. As J/ψ and $\Upsilon(1S)$ are the ground states and have smallest radius r_c, they will melt last at temperatures $T \sim 2T_c$ [4].

We should see this behaviour in the nuclear modification factor plot. In the Figure 1.8 on the left there is a scetch of sequential suppression for charmonia. The nuclear modification factor decreases with increasing temperature, and moreover, there are steps at temperatures when $r_D = r_c$ and corresponding type of charmonium is deconfined. We can see the behaviour of bottomia in real data from ALICE experiment on the Figure 1.8. The $\Upsilon(2S)$ is more suppressed than $\Upsilon(1S)$ because it is less bounded, so it deconfines at lower temperatures and its final production will be lower. Also there can be seen that as we are going to higher number of participants, that is, higher centralities and therefore higher probability to form a QGP, we can see more suppression of quarkonia.

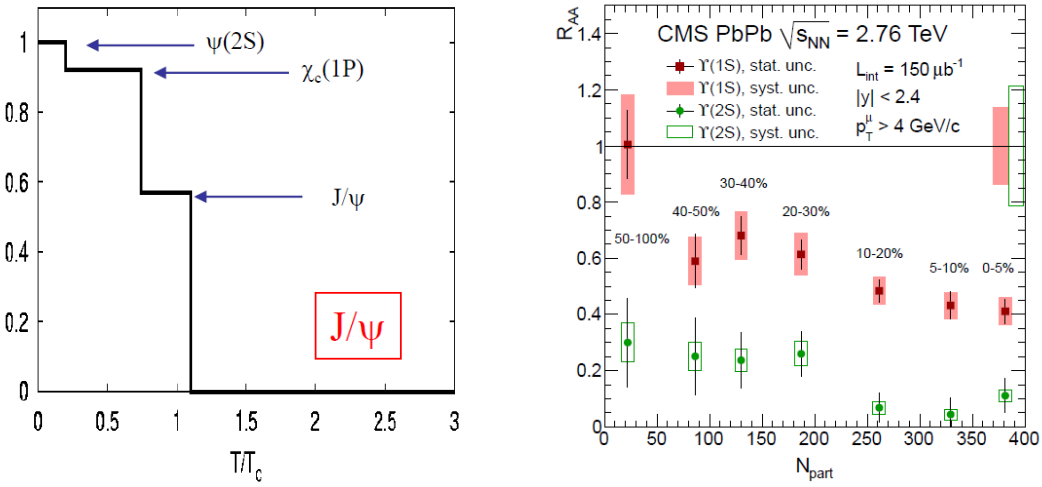

Figure 1.8: Left: Scetch of sequential suppression of different states of charmonia against T/T_c. Taken from [5]. Right: R_{AA} of $\Upsilon(1S)$ and $\Upsilon(2S)$ against centrality in Pb-Pb collisions at energy $\sqrt{s_{NN}} = 2,76$ TeV. Taken from [15].

Except the suppression caused by color screening in QGP, we can also observe the so called "normal suppression" of quarkonia observed in proton-nucleus collisions. This feature is caused by re-scattering dissociation of the primordially produced quark-antiquark pairs when traversing cold hadronic matter. We have to pay attention to this suppression in nucleus-nucleus collisions. In this case, the particle yield in AA collisions to "normal yield" is studied [4].

1.4.2 Open heavy flavor

Open heavy flavored particles are those composed of one c or b quark and one light quark. Among these particles there belong D and B mesons containing one charm quark and one bottom quark, respectively. In Table 1.2 there are some examples of D and B mesons, their masses and what quarks are they formed of.

meson	content	mass [MeV/c^2]	meson	content	mass [Mev/c^2]
D^0	c$\overline{u}$	1864,86	B^0	d$\overline{d}$	5279,58
D^+	c$\overline{d}$	1869,62	B^+	u$\overline{b}$	5279,25
D_s^+	c$\overline{s}$	1968,49	B_s^0	s$\overline{b}$	5366,77

Table 1.2: Properties of open heavy flavor mesons. Taken from [1].

An important part of the study of open heavy flavor is the suppression of high p_T particles caused by interactions of heavy quarks with quark-gluon plasma. According to dead-cone effect heavy quarks should lose less energy in this strongly interacting medium than light quarks because the gluon emission is suppressed in angles smaller than m/E. This should be seen in nuclear modification factor. The bigger the energy loss is, the smaller is the R_{AA}.

Ideally we should study the difference between nuclear modification factors of light, c and b quarks, that is of light hadrons, D and B mesons. Unfortunately the STAR experiment was not able to see tracks or even decay vertices of these mesons until year 2014. For that reason we have to rely on undirect measurement of daughter particles coming from decay vertices of open heavy flavor mesons.

D and B mesons can decay via hadronic or semileptonic decay channels. For hadronic decay channel of D mesons we select pions π and kaons K and by calculating their invariant mass we can get final distribution of these mesons. For hadronic decay channel of B mesons we select J/ψ coming from decay vertex. On the Figure 1.9 we can see the measurement of R_{AA} of light hadrons, D mesons obtained via hadronic decay channel analysis and B mesons analysed through decays to J/ψ from ALICE experiment in PbPb collisions at energy $\sqrt{s_{NN}} = 2,76$ TeV. According to dead-cone effect we should see the following relation: $R_{AA}^{ch} < R_{AA}^{c} < R_{AA}^{b}$. As ALICE experiment can recognize the decay vertices of open heavy flavor mesons, their analysis is more precise and so they claim that they can see an indication that this statement is approved.

On STAR experiment we have also measured the R_{AA} of D mesons via hadronic decay channel. On the Figure 1.10 there is the nuclear modification factor of D mesons compared to R_{AA} of light hadrons in AuAu collisions at energy $\sqrt{s_{NN}} = 200$ GeV. We do not see any difference between nuclear modification factors of light hadrons and D mesons beacuse of large error bars on the plot.

D and B mesons can also decay via semileptonic decay channel $D(B) \rightarrow e\nu_e X$. On STAR experiment we also perform this study of open heavy flavor. In this measurement we try to select electrons coming from the decay vertex of open heavy flavor mesons, called non-photonic electrons. It has one advatnage over the hadronic decay channel studies.

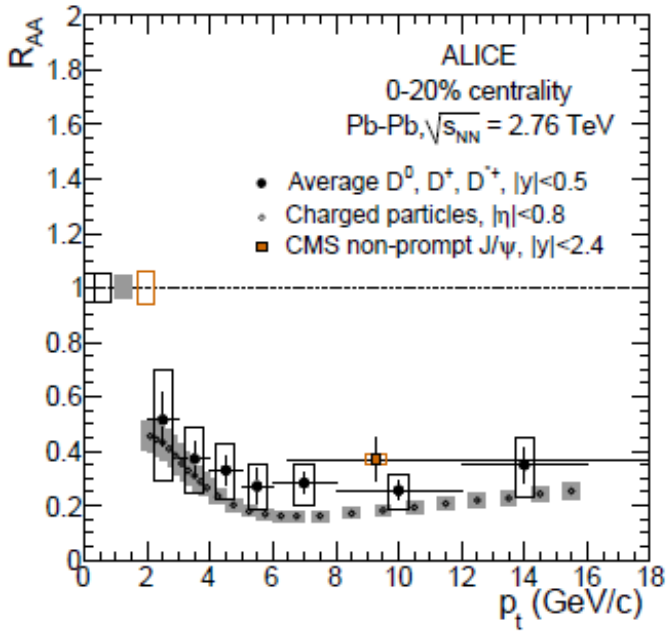

Figure 1.9: Nuclear modification factor of charged hadrons, D mesons and J/ψ coming from B mesons. The measurement is done by ALICE experiment in PbPb collisions at energy $\sqrt{s_{NN}} = 2,76$ TeV. Taken from [16].

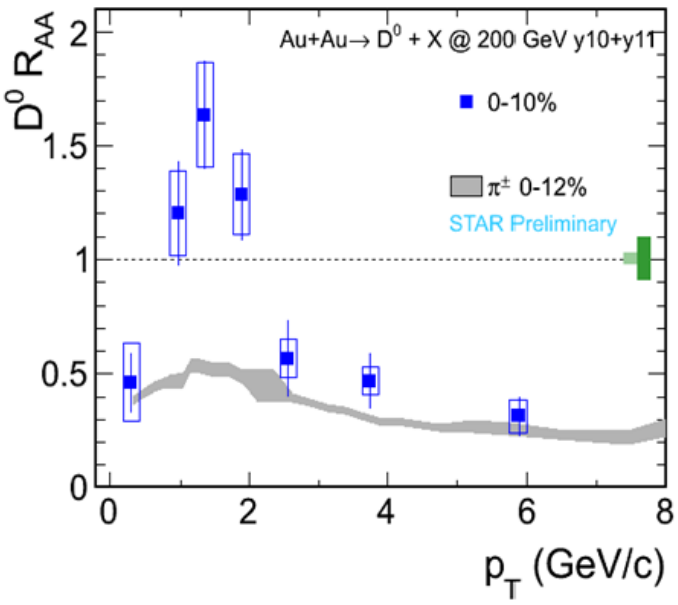

Figure 1.10: Nuclear modification factor of D mesons in central collisions compared to R_{AA} of light hadrons. Taken from [17].

During data taking we are able to trigger on high-energy electrons in the Electromagnetic Calorimeter. This kind of trigger is called NPE trigger. It is fired only when the Calorimeter detects a hit with a deposited energy higher than a certain threshold. However, this measurement has a lot of disadvantages too. Due to inability of detecting the neutrino we cannot reconstruct the invariant mass of D and B mesons which makes the analysis a little bit harder to perform. The momentum of the electron does not correspond to the momentum of D or B meson, so we cannot directly compare the R_{AA} with R_{AA} of other particles. The non-photonic electron spectrum is accompanied with a large background composed of electrons coming from γ conversions or decays of quarkonia. Also, the reconstructed NPE is a mixture of c and b quark contributions. This kind of analysis is the core of my research work.

Chapter 2

The STAR Experiment

The Solenoidal Tracker at RHIC is one of two detectors that are operating at Relativistic Heavy Ion Collider (RHIC). It is located at one of the six intersection points of RHIC beam pipes. It covers all azimuth around the beam pipe and is composed of various subsystems. The most important parts for heavy flavor physics are the Time Projection Chamber, Time of Flight, Barrel Electromagnetic Calorimeter and lately added new detectors Heavy Flavor Tracker and Muon Telescope Detector. A magnet is wraping them all except the MTD. The magnet is needed for creating a magnetic field of 0,5 T to bend trajectories of charged particles. A picture of the STAR detector is shown on the Figure 2.1.

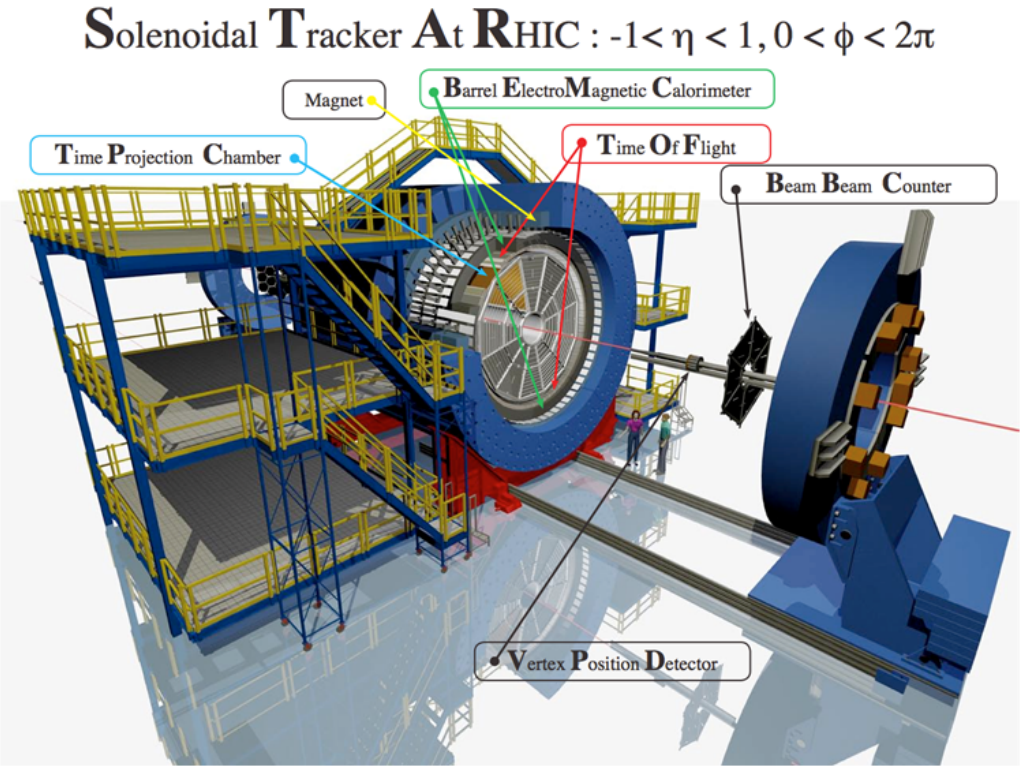

Figure 2.1: Picture of STAR detector.

2.1 Time Projection Chamber

The Time Projection Chamber is the main subdetector of STAR. It is designed to detect trajectories of particles and according to their energy loss help particle identification. TPC is cylindrically shaped gas detector with long response. Its inner radius is 50 cm and the outer radius 200 cm. It is 420 cm long and covers all azimuth 2π and pseudorapidity $|\eta| \leq 1$ [22]. It can distinguish pions from kaons up to $p \sim 0,6$ GeV/c, as can be seen from the picture 2.2.

When a particle traverses some material, it loses energy by ionization or radiation. In case of TPC the ionization losses are important and can be described by Bethe-Bloch formula [1]

$$-\langle\frac{dE}{dx}\rangle = K\frac{Z}{A}\frac{z^2}{\beta^2}[\frac{1}{2}ln\frac{2m_ec^2\gamma^2\beta^2T_{max}}{I^2} - \beta^2 - \frac{\delta(\beta\gamma)}{2}], \tag{2.1}$$

where K is a constant, Z and A are proton number and atomic number of the material respectively, z is proton number of incoming particle, I is mean excitation energy, T_{max} is maximum transfer energy for one collision and the last member $\delta(\beta\gamma)/2$ is a correction for density effects at high energies [1]. Every particle loses different amount of energy when traversing the same material. So by investigating the shape of Bethe-Bloch function we can perform particle identification. On Figure 2.2 an example of particle identification is shown. The colored curves are fits with Bethe-Bloch formula for different particles.

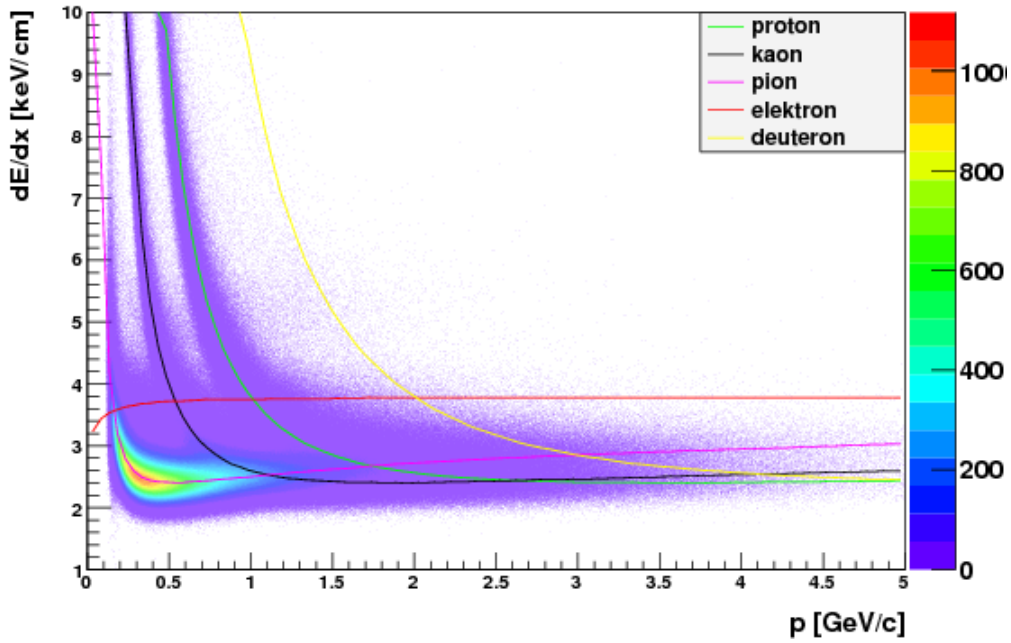

Figure 2.2: Energy loss as function of momentum. The colored curves represent a fit with Bethe-Bloch formula for different particles.

2.1.1 How does TPC work

Time Projection Chamber is composed of central high voltage cathode and of two anodes located at both sides. A schematic picture of TPC can be seen on Figure 2.3.

There is an electric field parallel to the beam pipe and also a parallel magnetic field created by the magnet that is wraping every subdetector of STAR except MTD inside. The

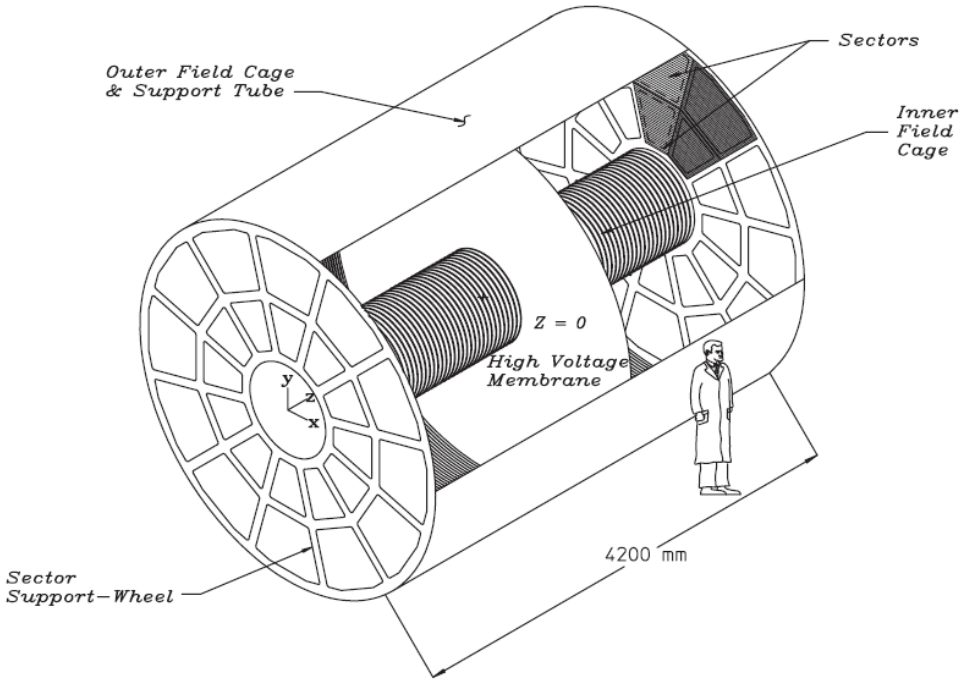

Figure 2.3: Time projection chamber. Taken from [20].

TPC is filled with gas, so when a particle traverses this medium, it ionizes the molecules of gas and electron-ion pairs are formed. Created charges are gathered by electrodes of corresponding opposite charge. Right before the anodes the electric field is stronger. Incoming electrons will then have enough energy to ionize the gas and create even more electron-ion pairs. A Townsend avalanches are created that are needed for signal readout. During avalanches there are a lot of positively charged ions created that cause the decrease of the intensity of electric field. For that reason there is a ground grid that collects positive ions and it also divides the space of avalanches from the rest of TPC [23].

Anodes consist of endcap wire chambers, where anode wires are distributed uniformly. Parallel to these wires there are series of cathode square stripes. This configuration allows us to determine the projection of particle track on $x - y$ plane. The x coordinate is obtained by the position on the anode wire, the y coordinate by a cathode strip from parallel line to the anode wire and finally the z coordinate is given by the time in which electrons reach the anode. By this way we obtain the points of a particle trajectory that we can reconstruct [23].

The gas that the TPC is filled with is a compound of 90% of Argon and 10% of Methan. The noble gas is good because it does not need to attach another electrons so we will not have problems with electron losses due to binding with molecules. The organic gas is important because it is able to quench UV photons so they do not cause molecule excitations and adjacent creation of electron-ion pairs. There will be a change of gas mixture from Argon-Methane to Helium(50%) and Ethane(50%) as it will increase the efficiency [20].

2.2 Time of Flight

The Time of Flight (TOF) detector is an important subsystem of STAR because it helps with particle identification. It is capable of distinguishing pions from kaons up to $p \sim 1,5$

GeV/c and protons from $p \sim 1$ GeV/c up to $p \sim 3$ GeV/c. In the Figure 2.4 en example of particle identification is shown. The colored curves represent a theoretical predictions of inverse β according to fromula 2.2. Comparing to Bethe-Bloch functions obtained from TPC 2.2 it is clear that TOF can distinguish better between the particles up to higher momentum than TPC.

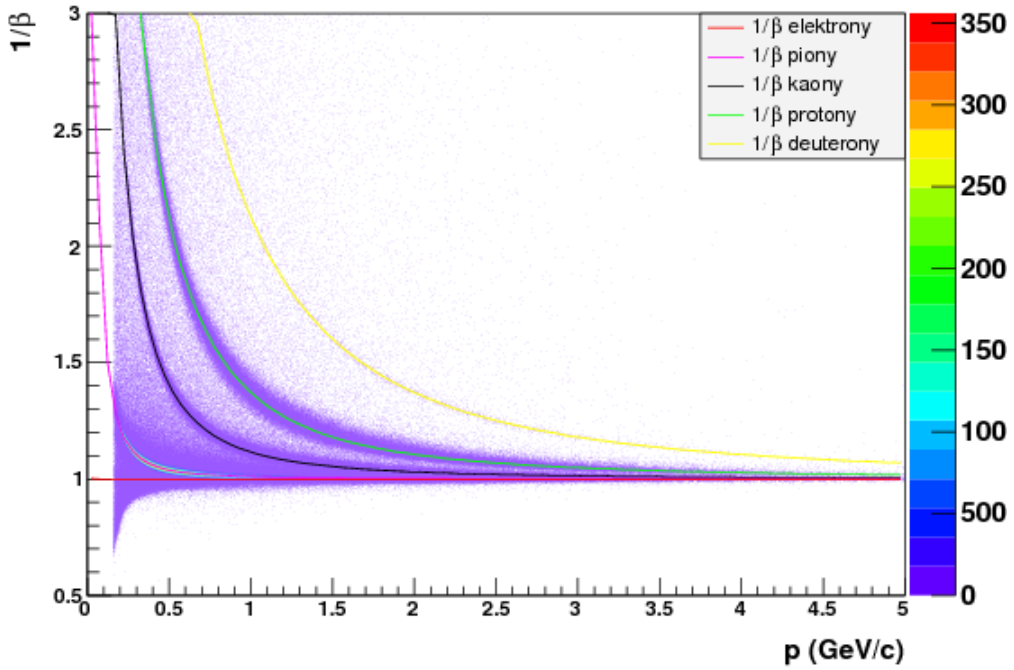

Figure 2.4: Particle identification from Time of Flight. The colored curves are theoretical values for calculation of the inverse β.

With TOF we can measure the time of flight of the particle, where the starting time is determined by Vertex Position Detector (VPD) and the end time by TOF. From the time difference and known distance the particle travels it is possible to calculate the velocity β. Together with the momentum obtained from TPC one can identify the particle, i.e. calculate its mass according to following formula [21]

$$m = p\sqrt{\frac{1}{\beta^2} - 1}. \tag{2.2}$$

The Time of Flight detector surronds the TPC, so it covers full azimuth 2π and pseudorapidity $|\eta| \leq 1$. It works on the base of Multi-gap Resistive Plate Chambers (MRPC) which has good time resolution around 100 ps and high detection efficiency of more than 95%.

2.3 Barrel Electromagnetic Calorimeter

The Barrel Electromagnetic Calorimeter (BEMC) is important part of STAR because it measures the energy of particles and it also serves for high-tower triggers. High-tower trigger is fired when there is an event with at least one hit with energy higher than some given value.

The BEMC again covers all azimuth 2π, pseudorapidity $|\eta| \leq 1$ and its inner radius is 220 cm. It consists of 120 calorimeter modules and each module is compoed of 40 towers so the entire BEMC has 4800 towers total. Inside every module there are lead and scintillator plates alternating. When particle passes through, in the lead plate a shower is created, and in the adjacent scintillator plate the signal is read out. There are also shower maximum detectors (SMD) at a distance of $5X_0$ from the front face. X_0 is radiation length i.e., the distance in which the electron loses its energy to $1/e$ of its original value. For the analysis of NPE the SMD detectors are important for electron identification. We distinguish the SMD detector in η direction and SMD detector in ϕ direction. These detectors are needed to provide good spatial resolution because the towers are larger than the size of EM shower. On the Figure 2.5 a picture of one BEMC module is shown.

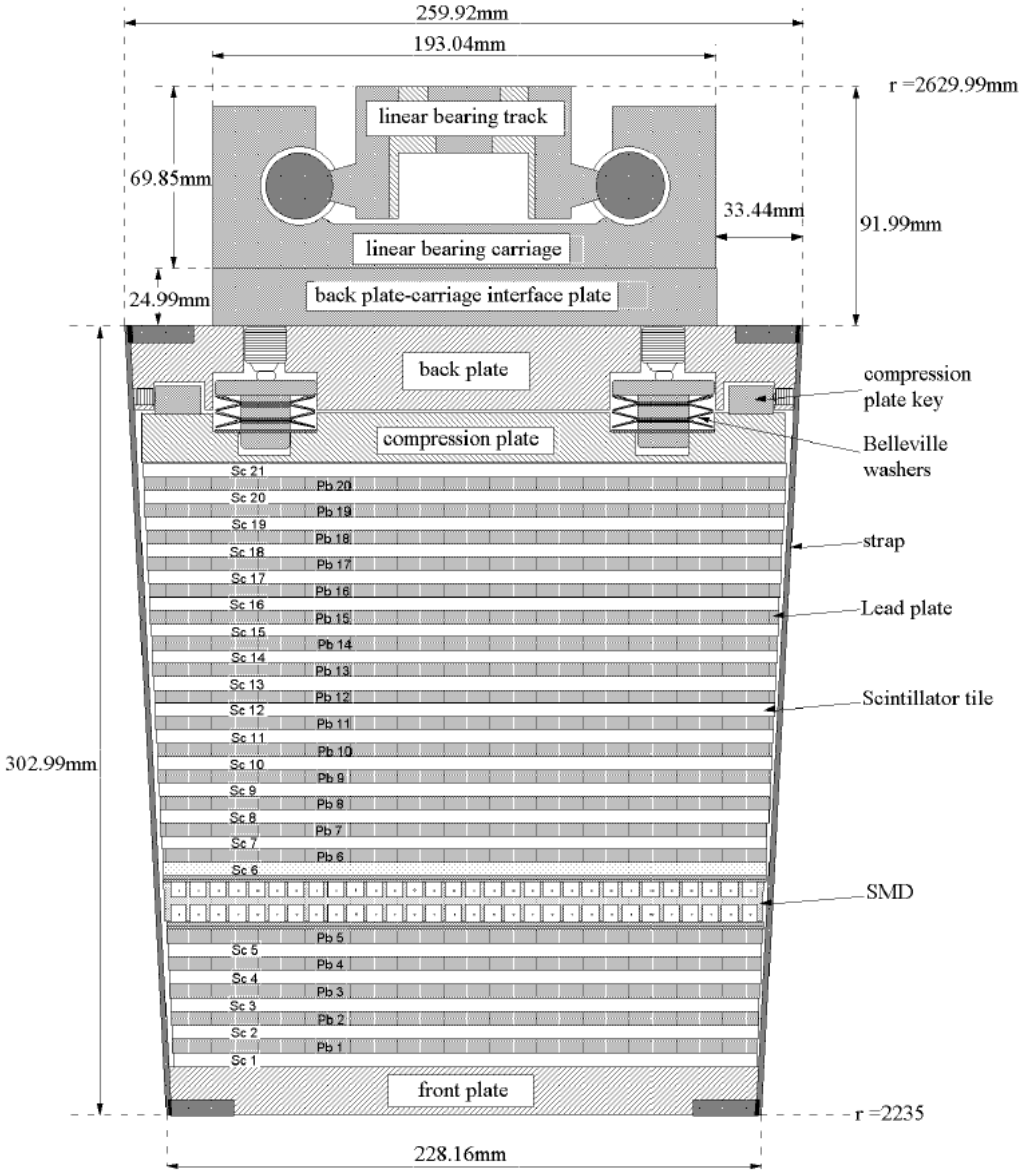

Figure 2.5: Picture of a module of BEMC Taken from [25].

2.4 Heavy Flavor Tracker

The Heavy Flavor Tracker is a silicon pixel detector, that is designed to improve the heavy flavor analysis. It will be able to distinguish decay vertices of D and B mesons, which will significantly help in the precision of the analysis i.e., the systematic errors will decrease. On the Figure 2.6 a scheme of this detector is shown. It is placed close to the beam pipe, and it consist of approximately 2 cm x 2 cm silicon plates [26]. On the Figure 2.7 there is a reconstruction of D^0 meson signal from simulation. Various selection criteria on secondary decay vertices of D meson are applied and are shown on different pictures. The signal is clearly visible among the background. We are not able to see such good signal in D meson reconstruction in present analysis.

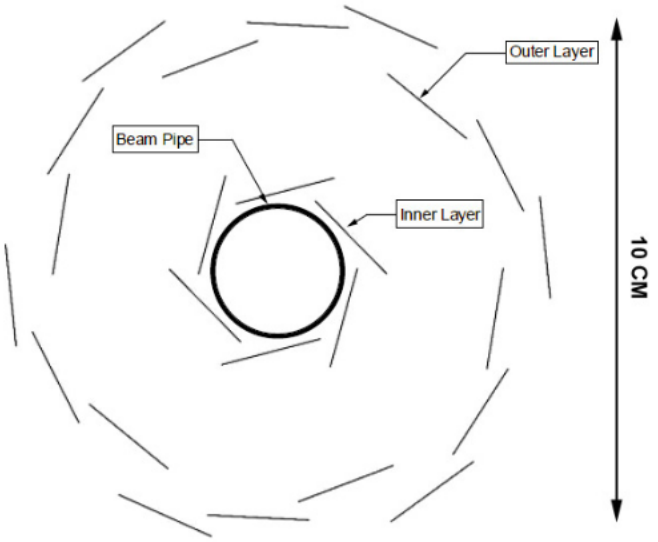

Figure 2.6: Scheme of Heavy Flavor Tracker - transverse cut. Taken from [26].

2.5 Muon Telescope Detector

The Muon Telescope Detector (MTD) is a newely installed detector that is located on top of the magnet. Main advantage of this detector is very low hadronic background due to its position. Mainly muons will pass through the magnet and steel backlegs to MTD almost without any hadron background, so we will be able to see clear peaks with low noise. An example is shown on the Figure 2.8. With MTD we can study J/ψ and Υ through muonic decay channel. Because of small background we will be able to distinguish between different Υ states.

The MTD detector will be placed 400 cm away from the interaction point on the steel backlegs. However MTD trays are not installed on all 30 backlegs because it was required to leave a free space for operations on BEMC. On 3 backlegs there are three trays located and on the others there are 5, so in total there are 117 trays of MTD. The time resolution is < 100 ps and spatial resolution is ~ 1 cm. MTD uses the same electronics as TOF do, namely LMRPC (Multi-gap Resistive Plate Chamber with Long Strips). MTD covers $\sim 40\%$ of azimuth and $|\eta| < 0,5$ [27].

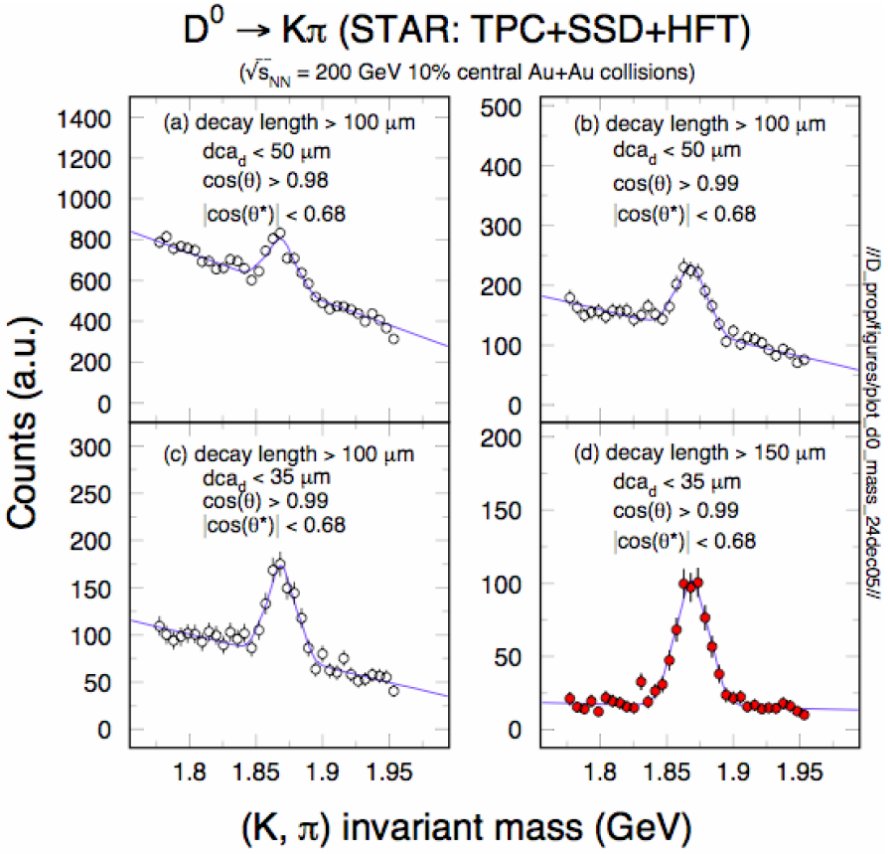

Figure 2.7: Reconstruction of D^0 meson signal with included HFT. Various selection topological criteria are applied. Taken from [26].

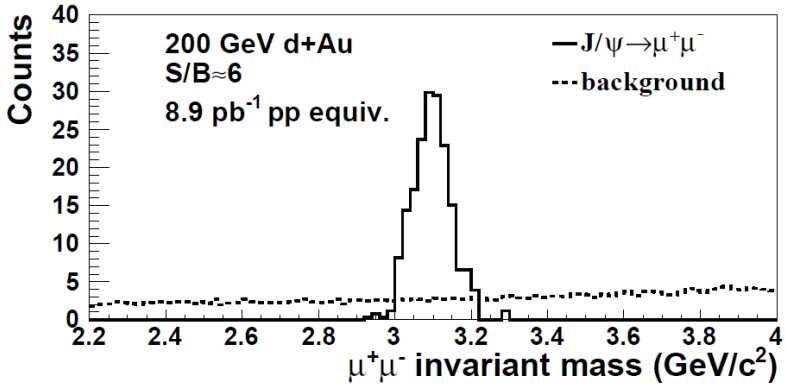

Figure 2.8: $J\psi$ signal as it would look like with MTD. Taken from [27].

Chapter 3

Measurements of Non-photonic electrons

Non-photonic electrons come from semileptonic decays of D and B mesons ($D, B \to l\nu_l X$). They are one of the good probes that can serve us in study of the quark-gluon plasma. Generally we divide all electrons that are created in a collision into two groups:

- Photonic electrons that always come out in pairs e^+e^-
  - Conversions γ: $\gamma \to e^- + e^+$
  - Dalitz decays, e.g. $\pi^0 \to e^+ + e^- + \gamma$, $\eta \to e^+ + e^- + \gamma$
- Non-photonic electrons produced together with (anti)neutrino through weak interaction of a $W^\pm$ boson
  - Decays of D and B mesons $D(B) \to e\nu_e X$

The analysis of non-photonic electrons is accompanied by large background coming from photonic electrons and electrons from Dalitz decay of π^0 and η mesons. It is a different way of studying open heavy flavor mesons (it can also be studied by reconstruction of π and K created in hadron channel decays of D and B mesons). In this analysis, however, we are not able to reconstruct directly the open heavy flavor mesons because we can't detect the neutrino coming from the decay vertex. Therefore we call it an indirect way of open heavy flavor study.

First step in the NPE analysis is to select all electrons that are produced in a collision i.e., inclusive electrons $N(inc)$. It is also necessary to extract the photonic electron yield $N(phe)$ which forms the above mentioned background. According to the relation 4.1 we get the raw non-photonic electron yield $N(npe)$.

$$N(npe) = N(inc).\epsilon_{purity} - N(pho)/\epsilon_{pho} \tag{3.1}$$

In this relation ϵ_{purity} is a purity that indicates the hadron contamination of the sample of inclusive electrons and ϵ_{pho} is the efficiency of photonic electrons reconstruction [28].

Second, the raw spectra have to be corrected on the cut efficiencies, and finally the contribution from vector mesons or J/ψ and Υ decays has to be subtracted.

The cross section of NPE can be calculated from the following relation [28]:

$$E\frac{d^3\sigma}{dp^3} = \frac{1}{\mathfrak{L}}\frac{1}{2\pi p_T \Delta p_T \Delta y}\frac{N_{npe}}{\epsilon_{rec}\epsilon_{trig}\epsilon_{eid}\epsilon_{BBC}}, \tag{3.2}$$

where N_{npe} is raw yield of non-photonic electrons, ϵ_{rec} is the product of the single electron reconstruction efficiency and the correction factor for momentum resolution and finifte spectrum bin width, ϵ_{trig} is the high-tower trigger efficiency, ϵ_{eid} is the electron identification efficiency, $\mathfrak{L}$ is the integrated luminosity and ϵ_{BBC} is the BBC trigger efficiency [28]. In NPE analysis using central triggers (which is the case of my analysis discussed in the last chapter 4) we don't need to divide the raw spectrum with trigger efficiency because we suppose the trigger is 100% efficient.

In the NPE analysis in heavy-ion collisions we are interested in the nuclear modification factor distribution because we expect a suppression pattern in high-p_T region. In my analysis of NPE in UU collisions at energy $\sqrt{s_{NN}} = 193$ GeV described below, I will only use the central triggers for 1% and 5% of the most central events. As NPE measurement in AuAu collisions have been already carried out, the physical motivation of NPE analysis in UU collisions is to compare the NPE yield in the most cental events with NPE yield in AuAu collisions and see if there will be a suppression or not. More about the motivation can be found in chapter 4.

3.1 B meson contribution

The selected NPE electrons can come either from D or B meson decays. The STAR detector didn't have any reliable detector to select the open heavy flavor mesons decay vertices until the year 2014. Therefore we have to rely on other methods that can disentangle the D and B contributions. To differ these contributions to the NPE cross section we use the electron-hadron azimuthal correlations. In the Figure 3.1 the FONLL calculations of corresponding contributions to NPE cross section are shown. It can be seen that under $p_T \sim 5$ GeV/c the charm contribution is dominant. At higher p_T the B meson contribution becomes larger than D meson contribution [30].

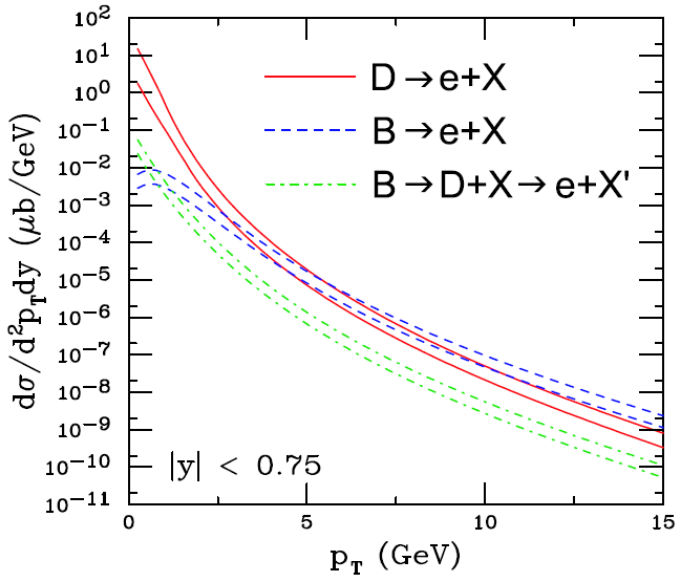

Figure 3.1: FONLL calculation fo D and B meson contributions to the NPE cross section. Taken from [30].

To separate charm and bottom contribution experimentally, azimuthal correlations between non-photonic electrons and hadrons are needed. One example of e-h correlations in 200 GeV pp collisions is shown in Figure 3.2. The correlation from B meson decay

have broader near-side peak ($\Delta\Phi \sim 0$) because as B meson have bigger mass, it can give more energy to its decay products. The data are fitted with a function that represents a combination of simulated charm and bottom distributions by PYHTIA [31]. The basic function shape is $y = x * D + (1 - x) * B$ where D and B are the relative contributions, and by adapting it to the data we can extract the parameter x.

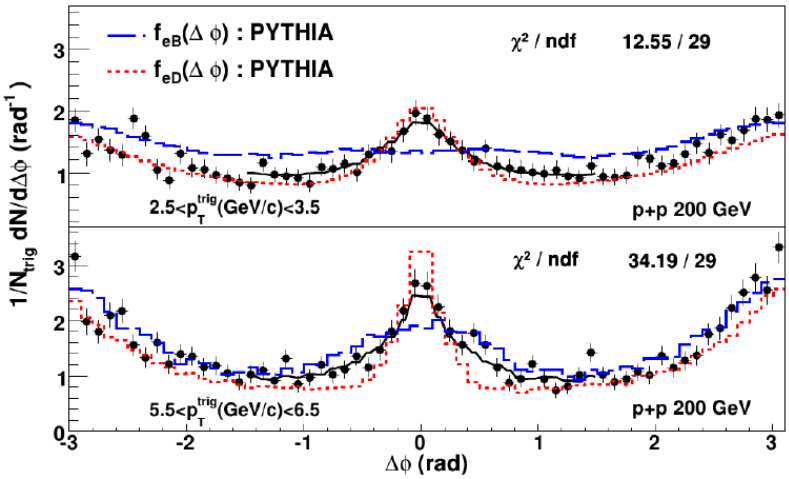

Figure 3.2: Non-photonic and hadron correlations in pp collisions at $E = 200$ GeV. Taken from [31].

Plotting the relative contribution of B mesons to all NPE yield, i.e. $B/(D+B)$ against p_T we can see the rise of bottom contribution with increasing p_T and also with increasing energy (see Figure 3.3), as was expected and discused above.

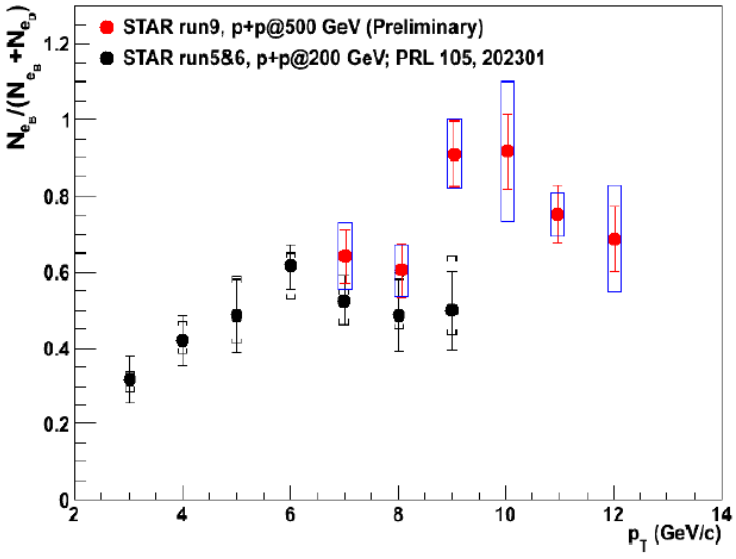

Figure 3.3: Relative bottom yield contribution to total NPE yield. Dependence on p_T and energy can be seen. Black points represent data from energy 200 GeV and red points from energy 500 GeV. Taken from [31].

3.2 NPE spectra in pp collisions

In this section I will present results from a STAR paper dedicated to the analysis of NPE in pp collisions at energy $\sqrt{s} = 200$ GeV from data taking in years 2005 and 2008. On the Figure 3.4 the NPE cross section is shown for combined run2005 and run2008 data together with run2003 data. Also the FONLL theoretical calculations are plotted with its uncertainties. For better comparison the ratio of data to theory is shown in the lower picture of the Figure 3.4. Results from PHENIX experiment are also shown. Data agree with FONLL within its uncertainties and are consistent with each other [28].

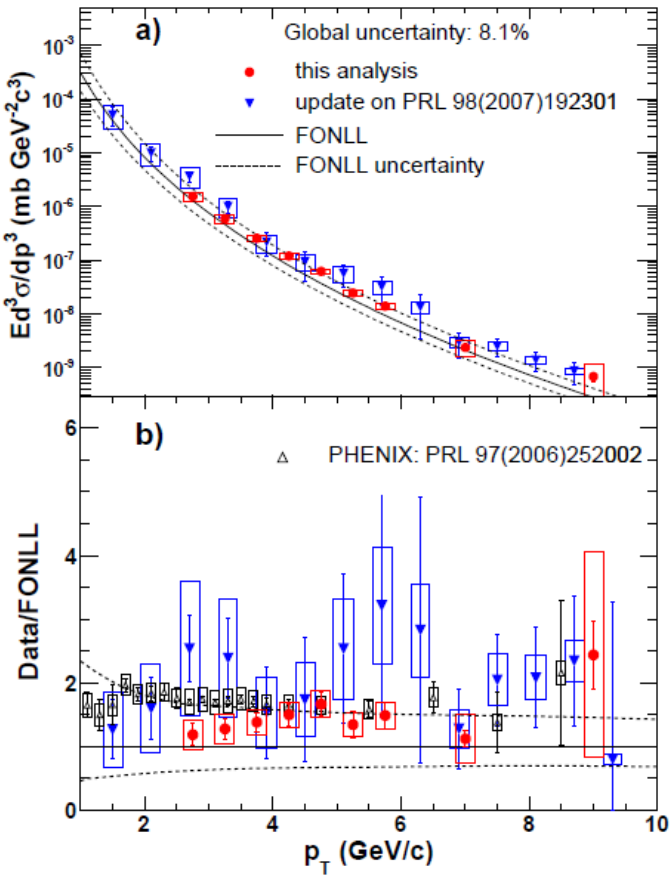

Figure 3.4: (a) Invariant cross section of NPE from combined run 2005 and run 2008 data together with corrected run 2003 results. Data are compared with FONLL theoretical calculations. (b) Ratio of data to theoretical predictions. Taken from [28]

After the calculation of B meson contribution to the NPE production, separate NPE cross section from D and B meson decays are shown on the Figure 3.5. The non-photonic electron cross section originating from B meson decays agrees well with FONLL calculations. The NPE cross section coming from D mesons is consistent with the upper boundary of theoretical calculations [28].

3.3 Suppression of non-photonic electrons

After extracting the NPE yield from heay-ion collisions, it should be compared to yield from pp collisions to see the degree of suppression. As it was mentioned in the chapter 1,

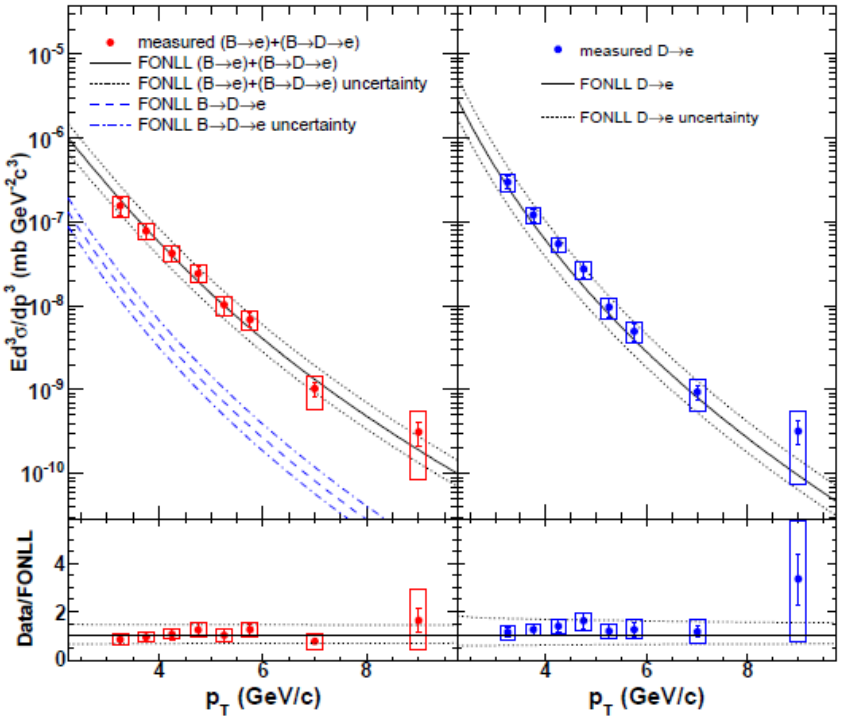

Figure 3.5: (Upper left: Invariant cross section of NPE coming from B mesons. Upper right: Invariant cross section of NPE originating from D mesons. Both data points are compared to FONLL calculations. Lower left and right: Ratio of data and theory. Taken from [28].

we expect smaller suppression of particles formed of heavy quarks than particles formed of light quarks i.e., $R_{AA}^{ch} < R_{AA}^{c} < R_{AA}^{b}$. I present here results from two different analysis of NPE in heavy-ion collisions in STAR experiment.

3.3.1 Au-Au collisions at $\sqrt{s_{NN}} = 200$ GeV, 2007

In the Erratum [34] from year 2011 there is nuclear modification factor of NPE in AuAu and dAu collisions at energy $\sqrt{s} = 200$ GeV plotted against p_T (see Figure 3.6). On the Figure 3.6 the R_{AB} of dAu collisions is consistent with the Cronin effect. This is an effect of cold nuclear matter caused by multiple scatterings in final stages of the collision.

The R_{AA} of NPE in AuAu collisions at $\sqrt{s_{NN}} = 200$ GeV is also shown on the Figure 3.6. The suppression of NPE does not differ much from suppression of light hadrons for $p_T > 6$ GeV/c that is shown as the grey band. There are also various models that try to describe the data. Curves I and II use radiative energy losses and they predict much less suppression than observed. Curve III and IV includes both radiative and collisional energy losses of heavy quarks. Curve V describes the radiative losses but only to D mesons. This curve describes data better because in these p_T ranges the D meson contribution dominates [34].

3.3.2 Au-Au collisions at $\sqrt{s_{NN}} = 200$ GeV, 2010

During run 2010, thanks to large statistics, we were able to divide the NPE yield in 5 centrality bins, see Figure 3.7. The production at pp collisions is fited with FONLL calculations. This yield is consistent with the upper limit of these calculations. The yields

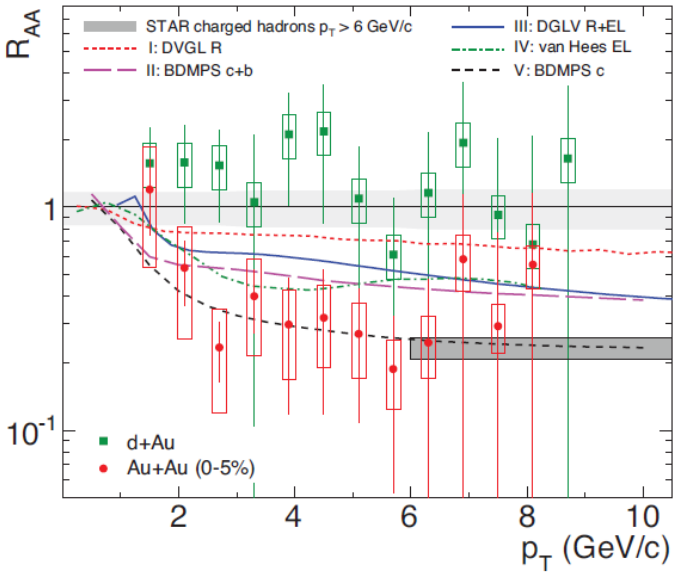

Figure 3.6: Nuclear modification factor of NPE in dAu and AuAu at $\sqrt{s} = 200$ GeV. Also the theoretical predicitons from various models are included. Taken from [34].

of NPE in different centralities are compared to pp produciton. i.e., the upper FONLL limit. It can be seen that with increasing centrality the NPE yield from heavy-ion collisions is getting lower in comparison with pp collisions.

The nuclear modification factor of NPE vs. p_T can be seen on Figure 3.8. The grey band represents the suppression of light hadrons and red points represent R_{AA} of NPE. The suppression of NPE is consistent with the suppression of light hadrons within the error bars. Also some theoretical models are included. Models that use only radiative energy loss do not describe the data well.

The amount of suppression of NPE seems to be much larger than we expected, actually almost the same as the suppression of ligh hadrons. Because of the dead-cone effect the suppression of heavy quarks should be lower than than of light quarks. Analyses that have been done until now do not have enough statistics to prove this statement. We also cannot divide relative D and B contributions to NPE because of low statistics. It is necessary to wait for new data [33].

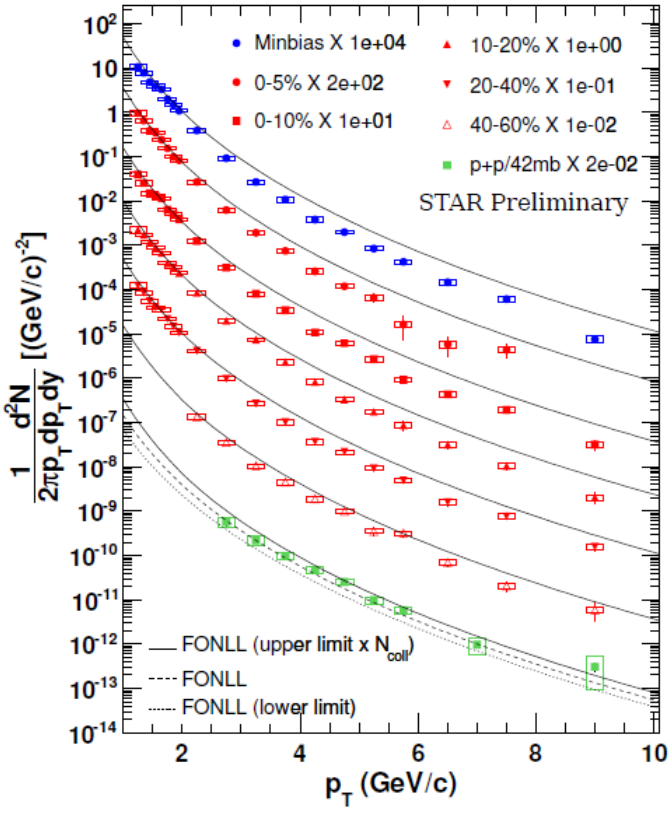

Figure 3.7: Invariant yield of NPE divided into 5 centrality bins. An invariant yield in pp collisions is plotted too. The yields are compared to upper limit of FONLL calculations. Taken from [33].

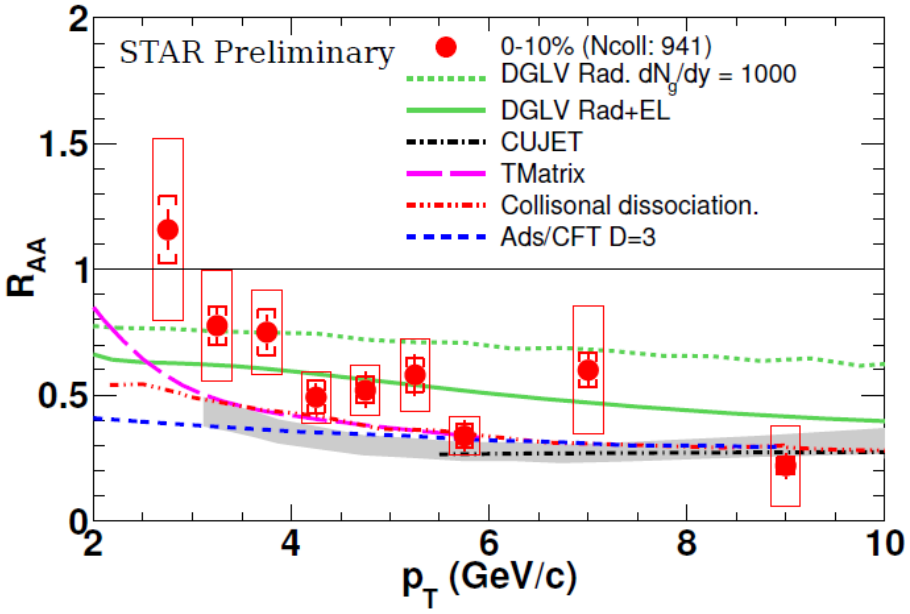

Figure 3.8: Nuclear modification factor of NPE together with various theoretical models. Also the suppression of light hadrons is included. Taken from [33].

Chapter 4

Analysis of non-photonic electrons

In this section I will describe my analysis of non-photonic electrons in UU collisions at energy $\sqrt{s_{NN}} = 193$ GeV in STAR experiment. The data were taken in year 2012. In my analysis I process the central triggers, namely the 1% and 5% of the most central events. I also analyze here only high p_T particles with $p_T > 1.2$ GeV/c. The plots presented in this chapter are obtained from 9,6 milion events. Due to lack of statistics, I plotted the figures only in 5 p_T bins from 1.2 GeV/c to 4 GeV/c.

The nucleus of Uranium is, in comparison to nucleus of Gold, deformed due to non-spherical charge density distribution that is, non zero quadrupole electric moment. For that reason we can accomplish various energy densities when colliding the Uranium nuclei at the same centrality. We can clasify the type of the collision of Uranium nuclei according to different rotation of nuclei. The first one is "tip-on-tip" which corresponds to situation when the main axis of a nucleus is parallel to the beam direction. The second one is called "body-on-body" when the main axis of nucleus is perpendicular to the beam direction. In the "tip-on-tip" collisions we can achieve higher partile multiplicity and energy density, and thus the formation of QGP is more probable [35].

The physical reason why I have chosen triggers mentioned above is that at these very central events we suppose that almost all collisions are "tip-on-tip", so we will deal with about 30 % higher energy denisty [35]. For that reason we expect that the suppression of high-p$_T$ particles will be higher with respect to other nucleus-nulceus collisions using more symmetric nuclei.

4.1 Selection of Inclusive electrons

As was already mentioned in previous chapter, production of non-photonic electrons is computed according the following formula:

$$N(npe) = N(inc).\epsilon_{purity} - N(pho)/\epsilon_{pho}. \tag{4.1}$$

First task is then to get the inclusive electron sample, which means to extract all electrons that are created in a collision. For this we need to apply first some event cuts. I want the event to occur at the centre of the STAR detector so that all tracks coming from that event will be in the detector acceptance. For this reason I apply a cut for event vertex position along the z direction: $|V_z| < 30$ cm. The event vertex is located via reconstruction of tracks in the TPC which are then extrapolated to find a point from which they originate. This method is however not very precise. Therefore I use another cut on difference between the position of event vertex obtained from TPC and VPD detector which can also locate the event vertex. The applied cut is $|V_z^{TPC} - V_z^{VPD}| < 3$ cm. On

the Figure 4.1 the distributions of V_z from TPC and the difference between position of vertices from TPC and VPD are shown.

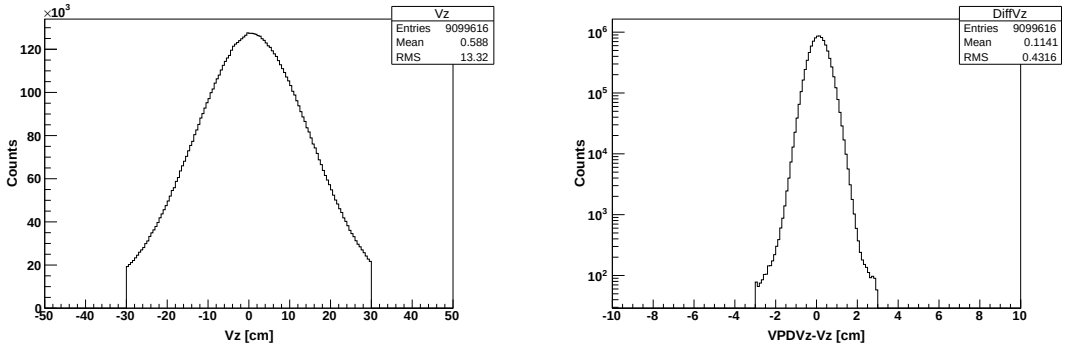

Figure 4.1: Left. Distribution of event vertices. Right: Distribution of the difference between the position of event vertices obtained from TPC and VPD detectors.

After the selection of good events I can procced to trajectory cuts. First I cut on the transverse momentum of tracks $p_T > 1.2$ GeV/c. As I want to study the suppression of high-p$_T$ particles, I don't need to include the low-p$_T$ ones yet. Another reason is that in the analysis of low-p$_T$ particles it is very hard to distinguish non-photonic electrons.

I applied another cuts on the track quality reconstruction in TPC detector. Tracks are reconstructed on the basis of fitting the points that are created by gas ionization in the TPC chamber. I required the track to have nHits ≥ 20 so that the fit would be trustworthy. Another cut on the ratio of fitted points to the maximum number of points nHits/nPossHits > 0.52 is applied. This is to avoid the double counting of one trajectory: Sometimes the trajectory points can be splitted and read out as two different trajectories which leads to small nHits/nPossHits ratio. I also used a cut on the so called number of dEdx hits in TPC. Not all points that are used to fit the trajectory have ideal signal and for that reason not all TPC points are used for the calculation of the particle's energy loss. The cut I applied is thus dEdxHits ≥ 15.

Trajectories that I use have to originate in the same event vertex and for this reason a cut for distance of the closest approach of the track to the vertex is used. As the vertex is obtained by track extrapolation, they don't need to end up directly at one point. However those that really originate in the vertex should be at least close to it. Thus I apply a cut $|\text{DCA}| < 1.5$ cm.

The pseudorapidity of tracks has to be $|\eta| < 0.7$ because I want to be sure that the track will fall in the detector acceptance and therefore it will be fully detected in TPC and also in the BEMC. The last trajectory cut is applied on the first point in TPC detector in transverse direction. As non-photonic electrons will originate almost directly at the collision point, I want to avoid tracks that are created in the gas chamber mostly due to γ conversions. So the cut applied is firstPoint < 73 cm.

4.1.1 Electron identification cuts

The cuts described above were only for track quality assurance. When I want to select the electron tracks, I have to use the specific ionization energy loss in the TPC chamber.

The normalized energy loss is defined as 4.2

$$n\sigma_e = \frac{ln\frac{\langle dE/dx\rangle^{mea}}{dE/dx^{th}}}{\sigma_{dE/dx}}, \tag{4.2}$$

where the indices "mea" and "th" mean measured and theoretical values, respectively. $\sigma_{dE/dx}$ is the experimental uncertainty. The normalized dEdx distribution should have a Gaussian pattern centered around 0. However, I use a cut $-0.5 < n\sigma_e < 2.5$, because at negative values there is a large contamination coming from pions.

The rest of electron identification cuts are using the information from BEMC detector. A clustering algorythm was used to group together 4 towers that are closest to the one tower that was actually fired by a particle. We call this group of towers a BEMC point. In the algorythm we project a track toward BEMC. We determine then the energy of the most energetic tower, the adc value of this tower and its SoftId and also the positions of SMDs from projected track and actually fired SMDs. The cuts that I am about to describe below, were determined using the pure electron sample, which can be accomplished by reconstruction of photonic electrons. To obtain the photonic sample, I loop first over primary tracks on which I applied all electron identification cuts, and then loop over global tracks. On the global partner track I used very mild cuts, that are: nHits $\geq$ 20, nHits/nPossHitss > 0.52, $p_T > 0.2$ GeV, $|n\sigma_e| < 3$. Normally the tracking cuts are not applied on global partner tracks, but in heavy-ion collisions they are needed so that the photonic electron tracks are not lost in very high background. Electrons that are created in γ conversions are always in pairs with very small invariant mass and also with opposite charges. I reconstructed first pairs with unlike sign, then pairs with like sign, which should describe background very well, and then I subtracted the like sign pairs from the unlike sign ones. When I apply additional cuts on invariant mass $m_{ee} < 0.24$ GeV/c^2 and on the distance of closest approach of the pair |pDCA| < 1 cm, I should get pure photonic electrons spample, on which I can study the EMC electron identification cuts as follows.

As electron is a very light particle and almost all of its energy is deposited in the calorimeter, I apply a hadron rejection cut $0.3 <$ p/E0 < 2, where $E0$ is the energy of the most energetic tower from the BEMC point. On the Fig. 4.2 the p/E0 cut is shown in various p_T bins.

In this analysis, also SMDs are used to determine electron tracks. These detectors are distributed in η and φ direction. We denote them as SMDE and SMDP, respectively. I don't want a track on which I can't apply cuts using SMD, so first thing is to constrain the tracks to have more than 1 hit in both SMDE snd SMDP detectors.

When projecting a track toward BEMC using the clustering algorythm, the result is not always perfectly matched with actually fired SMDs. I applied a cut on difference between the projected track SMDE and actually fired SMDE in η (z) direction, and between the projected track SMDP and actually fired SMDP in φ direction. As SMDE has good resolution only along the η direction and SMDP only along φ direction, it is not needed to cut on difference between SMDE in φ direction, or SMDP in η direction. On the Figure 4.3 are shown Δ_Z distributions for various p_T bins for like-sign pairs, unlike-sign pairs, and unlike-like pairs, which correspond to pure electron sample. On the Figure 4.4 the Δ_φ distributions are shown. I used SMD cuts as follows: $|\Delta_Z| < 0.3$ cm and $|\Delta_\varphi| < 0.015$ rad.

4.1.2 Photonic electrons sample

After the BEMC cuts determination I have to verify that I get a pure electron sample with these cuts. There are two ways of verifying this. First is to look at the invariant mass

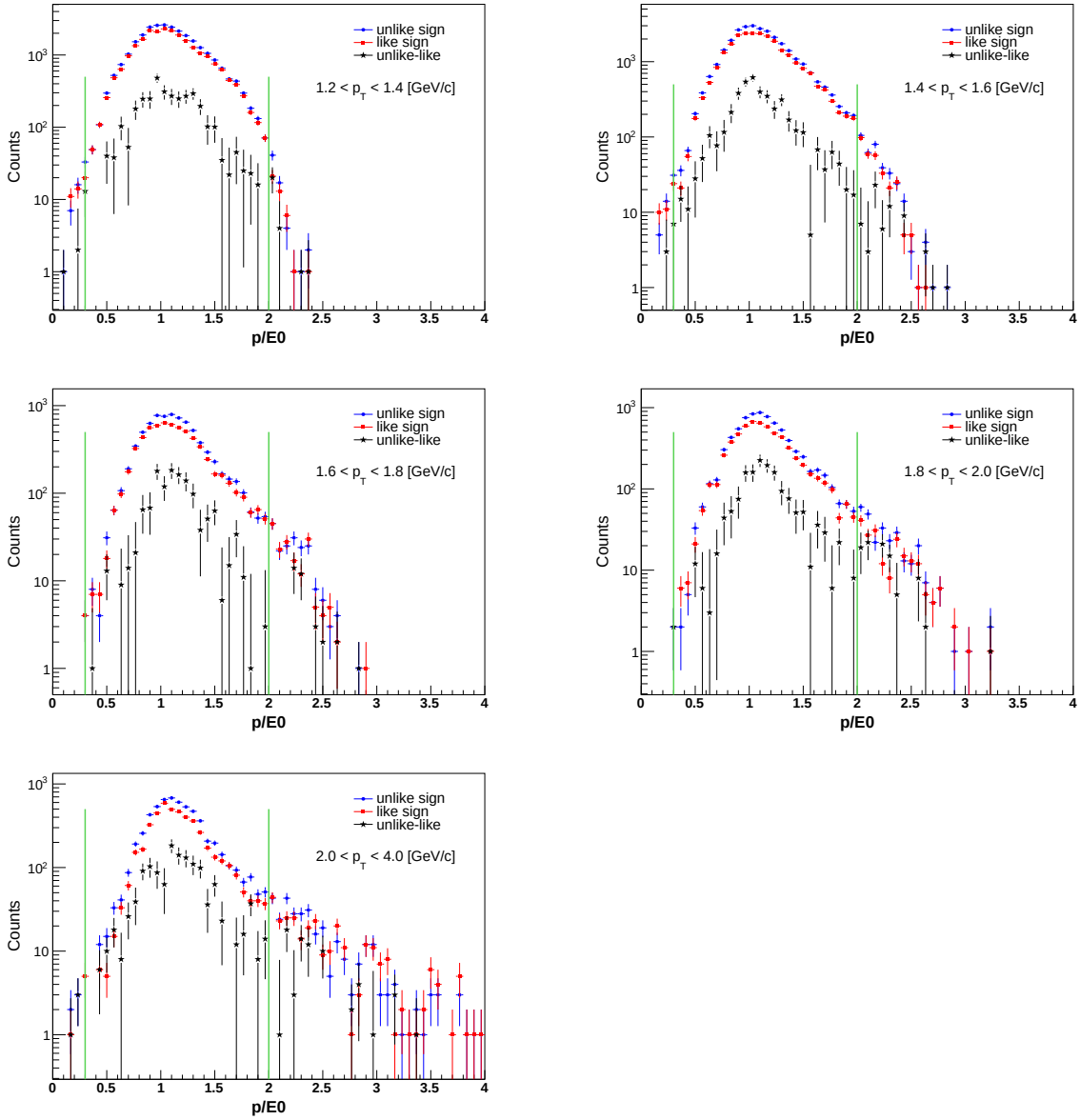

Figure 4.2: Distribution of $p/E0$ for unlike sign electron pairs (blue dots), like sign electron pairs (red dots) and the unlike-like sign pairs (black stars).

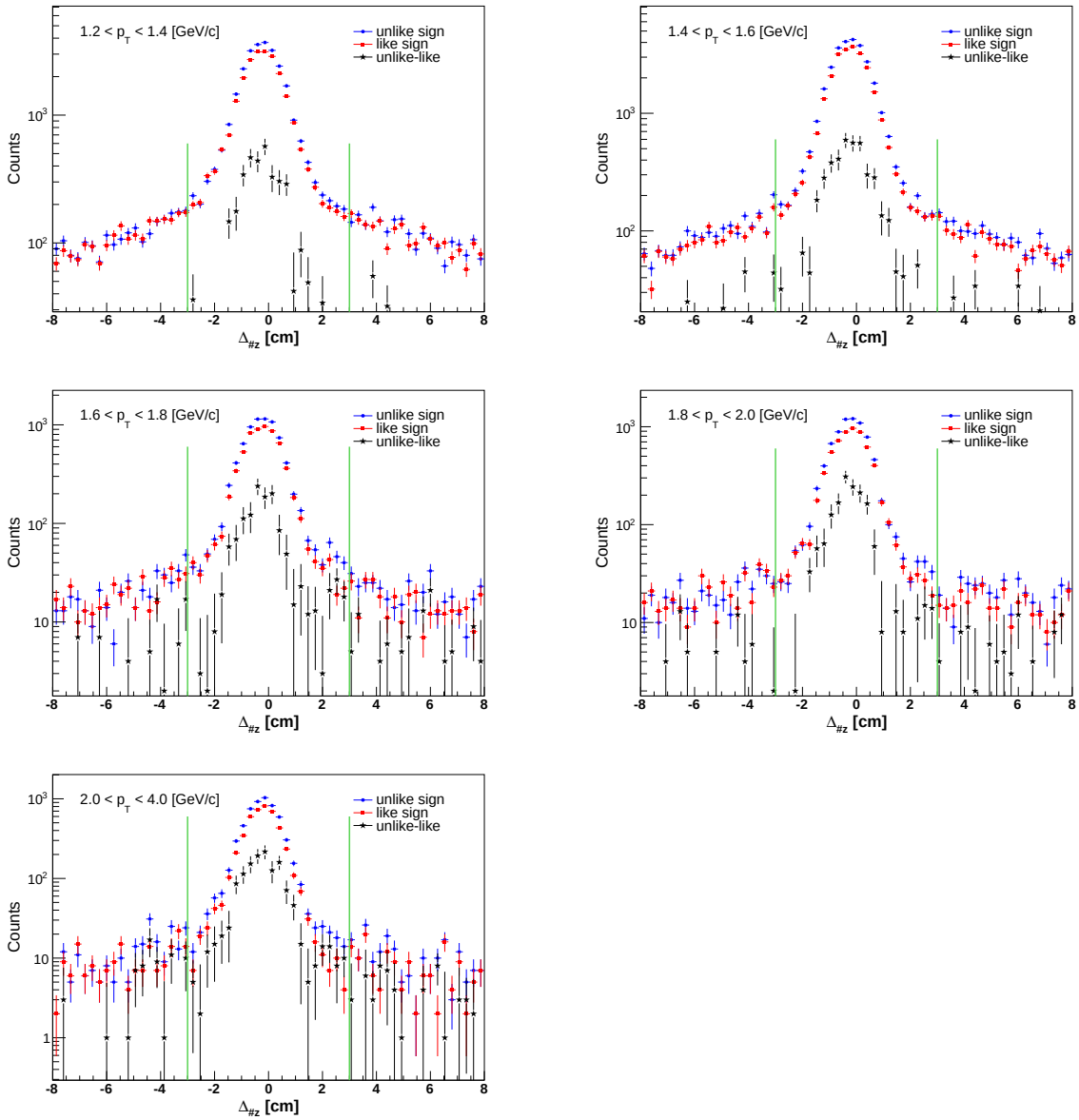

Figure 4.3: Distribution of difference between the projected track SMDE and actually fired SMDE in η direction for unlike sign electron pairs (blue dots), like sign electron pairs (red dots) and the unlike-like sign pairs (black stars).

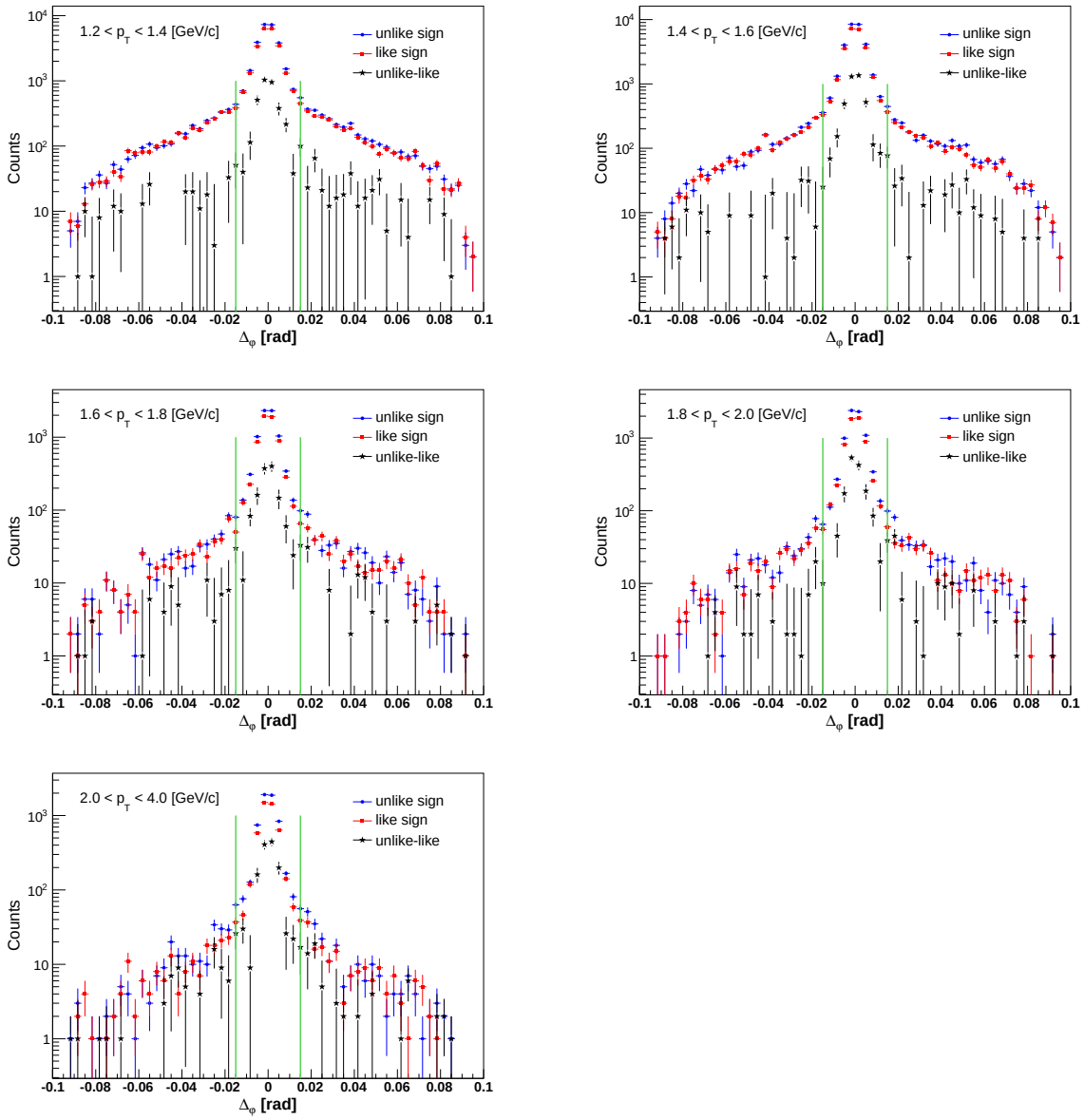

Figure 4.4: Distribution of difference between the projected track SMDP and actually fired SMDP in φ direction for unlike sign electron pairs (blue dots), like sign electron pairs (red dots) and the unlike-like sign pairs (black stars).

distribution for unlike sign, like sign and unlike-like sign pairs. Photonic electrons come from γ conversion or Dalitz decays of π^0 and η. The invariant mass of these electrons shouldn't be higher than 0.24 GeV/c^2. The like sign distribution of invariant mass should completely describe the combinatorial background, thus after subtracting the like sign pairs from the unlike sign pairs, the region of high invariant mass ($m_{ee} > 0.24$ GeV/c^2) should be equal to zero. On the Figure 4.5 the invariant mass distributions are shown for various p_T bins. It can be clearly seen that the like sign distribution describes the background well: the unlike-like sign point are fluctuating around zero at high m_{ee}.

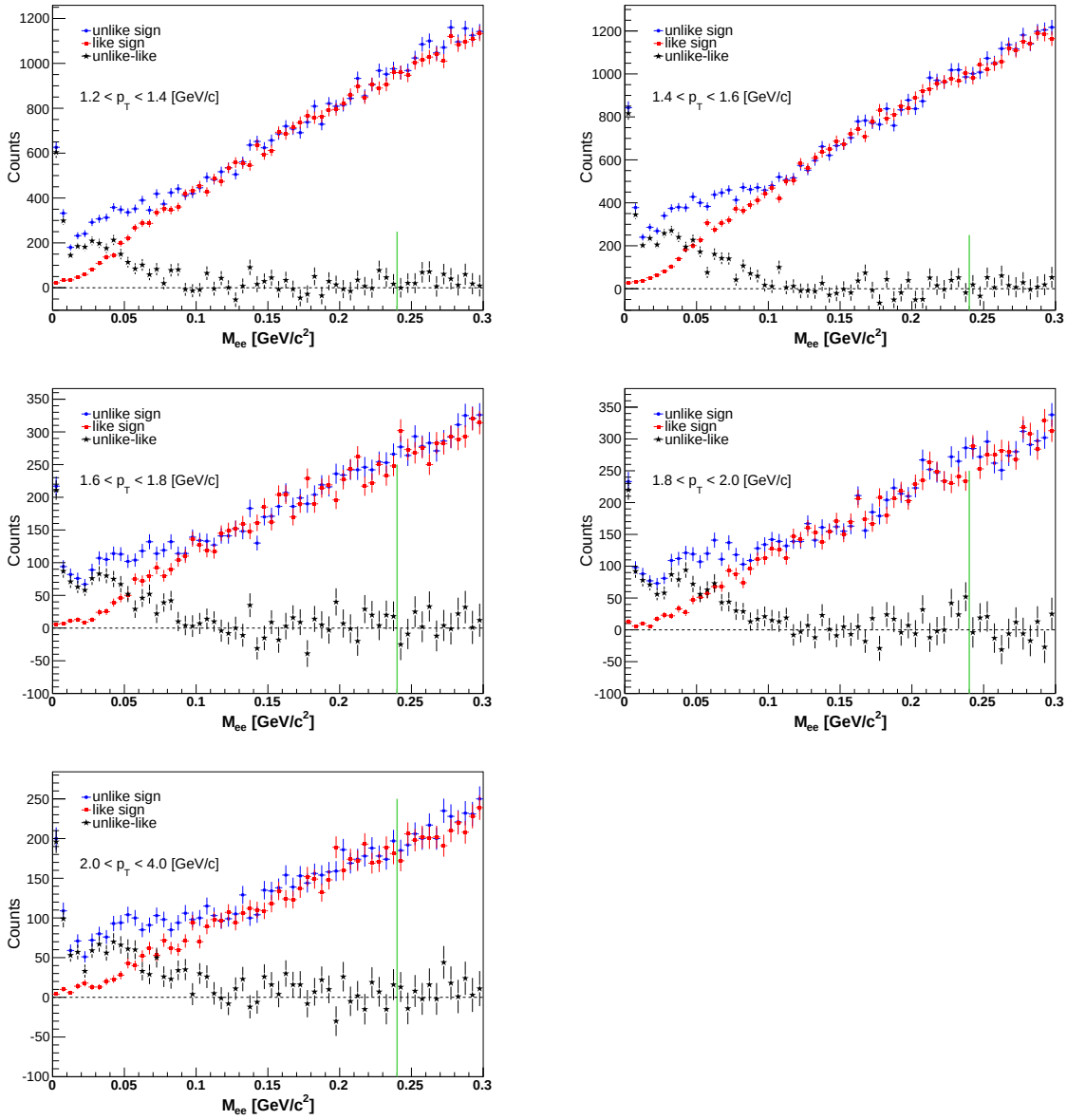

Figure 4.5: Distribution of electron pairs invariant mass for unlike sign (blue dots), like sign electron pairs (red dots) and the unlike-like sign pairs (black stars) for different p_T bins.

The second method for checking the pure photonic electron sample is to plot the $n\sigma_e$ distribution of the global partner track of a pair for unlike sign, like sign and unlike-like sign pairs. After all electron identification cuts the unlike-like sign distribution should follow a

perfect Gaussian. On the Figure 4.6 $n\sigma_e$ distribution of the global partner electron track is plotted in various p_T bins. The unlike-like distributions are fitted with Gaussian. As can be seen from the parameters of the fit, the unlike-like distributions follow a Gaussian very well, although the mean is shifted towards negative numbers, which is caused by bad calibration.

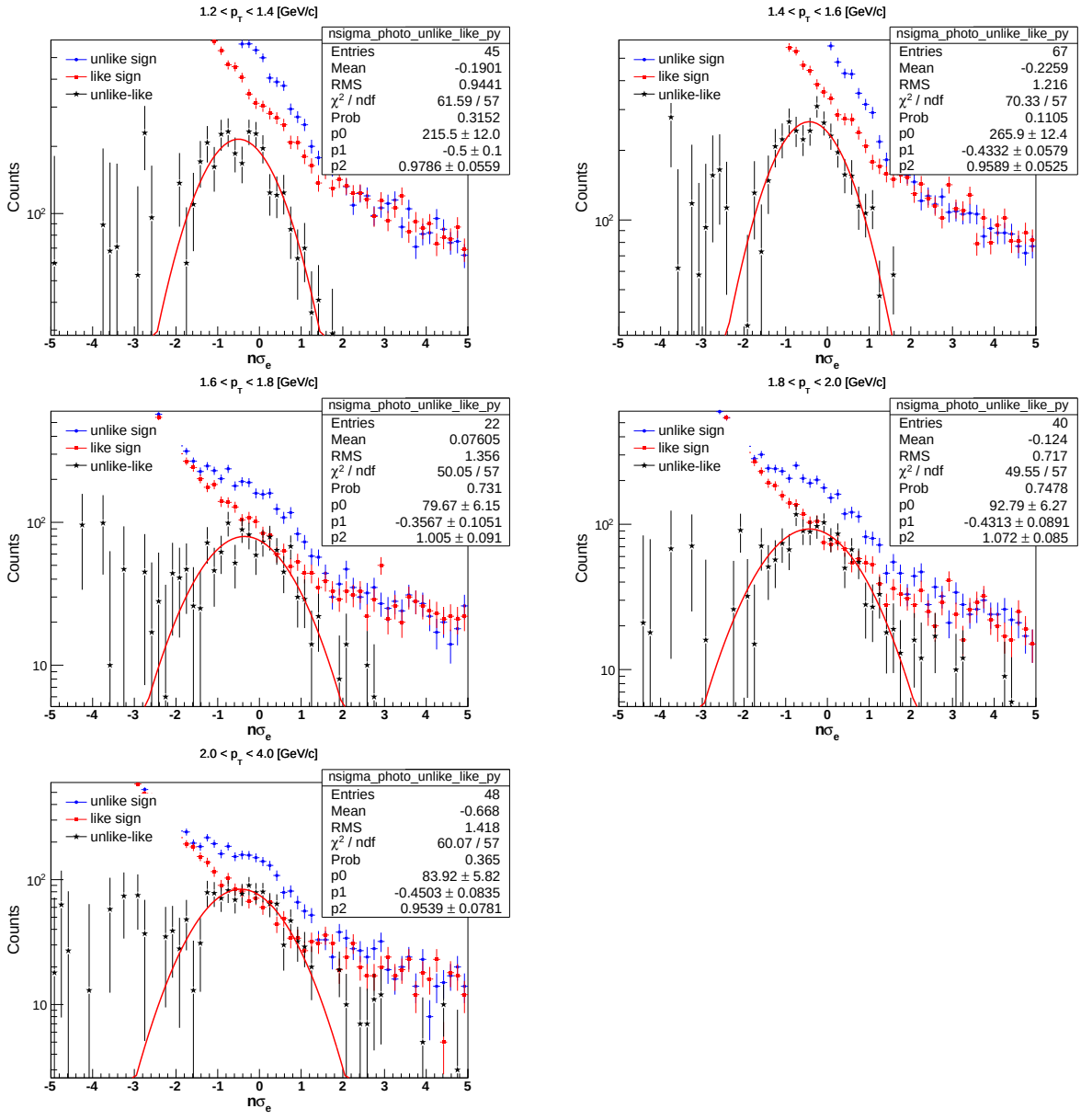

Figure 4.6: Distribution of $n\sigma_e$ of the global partner track for unlike sign (blue dots), like sign electron pairs (red dots) and the unlike-like sign pairs (black stars) for different p_T bins.

4.1.3 Summary of cuts applied in NPE analysis

In the Table 4.1 there is a summary of all cuts I have applied in the analysis of non-photonic electrons in UU collisions at energy $\sqrt{s_{NN}} = 193$ GeV.

Using the above mentiones cuts a raw p_T spectrum of the inclusive electron sample and the photonic electron sample can be drawn. The plot can be found on the Fig. 4.7.

Event cuts	
$\lvert V_z \rvert < 30$ cm	$\lvert V_z^{TPC} - V_z^{VPD} \rvert < 3$ cm
Track cuts	
nHits ≥ 20	$\frac{\text{nHits}}{\text{nPossHits}} > 0.52$
dEdxHits ≥ 15	$p_T > 1.2$ GeV/c
$\lvert \eta \rvert < 0.7$	firstPoint < 73 cm
Electron identification cuts	
$\lvert \Delta_Z \rvert < 3$ cm	$\lvert \Delta_\varphi \rvert < 0.015$ rad
$0.3 <$ p/E0 < 2	$-0.5 < n\sigma_e < 2.5$
nSMDE > 1	nSMDP > 1
Global Partner Cuts	
$p_T > 0.2$ GeV/c	$\lvert n\sigma_e \rvert < 3$
nHits ≥ 20	$\frac{\text{nHits}}{\text{nPossHits}} > 0.52$
Pair cuts	
$\lvert$pDCA$\rvert < 1$ cm	$m_{ee} < 0.24$ GeV/c^2

Table 4.1: Sumary of all cuts applied in the analysis of non-photonic electrons in UU collisions at energy $\sqrt{s_{NN}} = 193$ GeV.

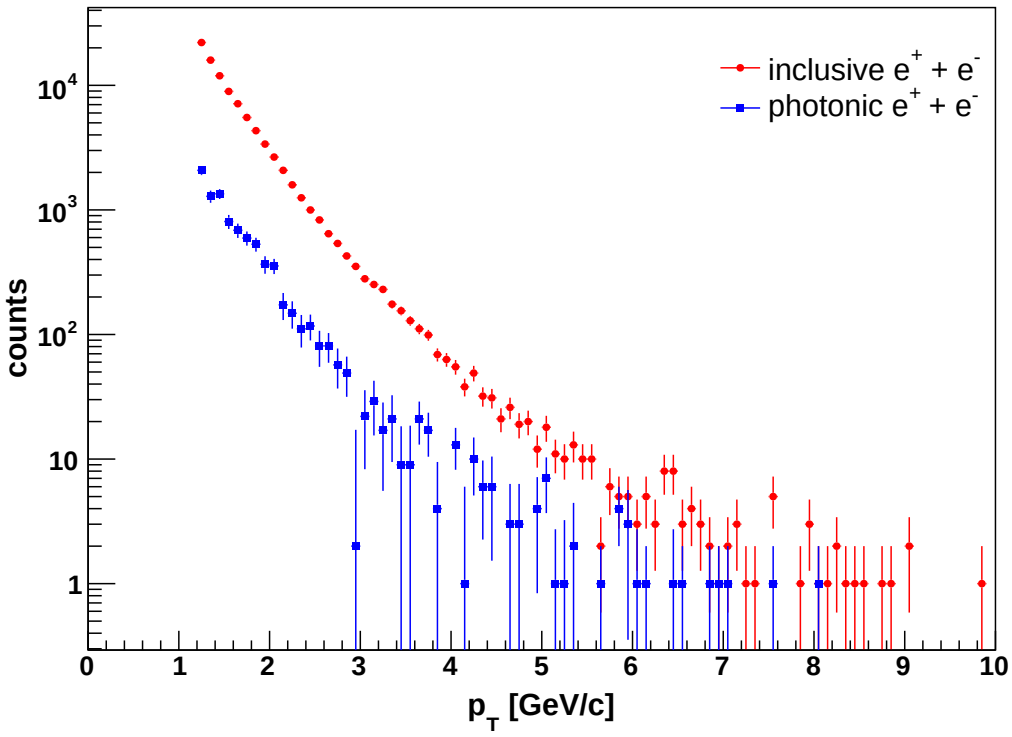

Figure 4.7: Raw p_T spectrum of the inclusive and photonic electron sample.

4.2 Efficiency calculation

By selection of electron tracks we are not able to select all tracks that are created in a collision. It is hard to reject the hadron contamination of the electron sample, as can be seen for example in the $n\sigma_e$ distributions of the global partner tracks of photonic electrons (Figure 4.6), where there is a large π contamination. We have to decide well if we cut on $|n\sigma_e| < 3$ with many π tracks included, or we cut $-0.5 < n\sigma_e < 2.5$ and then loose many of real electron tracks. For these reasons I have to correct the final distributions of non-photonic electrons using the efficiencies of cuts I applied during the electron tracks selection.

4.2.1 $n\sigma_e$ efficiency

For calculation of $n\sigma_e$ cut efficiency I use the distributions of $n\sigma_e$ of the primary electron track of photonic electron pairs in various p_T bins. I applied all cuts except the $n\sigma_e$ cut on primary electron track. If I don't have this cut, a large hadron contamination will appear. Therefore, to make sure that I will still have pure photonic electron sample, I use much tighter cut on the invariant mass and on $n\sigma_e$ of the global partner electron track: $m_{ee} < 0.01$ GeV/c^2, $-1 < n\sigma_e(\text{global}) < 3$. On the Figure 4.8 there are plots of $n\sigma_e$ of the primary electron tracks of photonic electron pairs in various p_T bins, fitted with a Gaussian function.

The efficiency of $n\sigma_e$ cut is calculated then as the ratio of electrons that pass the $n\sigma_e$ cut to all electrons without this cut. It can be achieved by dividing the integral under the Gaussian fit from $n\sigma_e = -0.5$ to $n\sigma_e = 2.5$ by integral in between $|n\sigma_e| < 5$ where I am sure it will contain all electrons. On the Figure 4.9 the $n\sigma_e$ efficiency is shown as a function of p_T.

The $n\sigma_e$ distribution of the primary electron track of photonic electron pairs are also used for calibration studies. Due to bad calibration during data taking, the $n\sigma_e$ distribution does not have its mean at 0, but it is shifted towards negative values. Therefore, I have to fit it with Gaussian and obtain the mean a width values of the distribution from the fit, which I will use later for purity estimation.

On the Figure 4.10 means and widths of Gaussian fits of $n\sigma_e$ distributions in various p_T bins are shown. The plots look reasonable, the widths are around 1 and the mean is shifted to $n\sigma_e = -0.4$.

4.2.2 EMC efficiency

Efficiency of the cuts using BEMC detector is calculated together due to possible correlations between them. The efficiency is calculated as the ratio of electron yield after the EMC cuts to electron yield without EMC cuts. The EMC cuts I used in this analysis are: $|\Delta_Z| < 3$ cm, $|\Delta_\varphi| < 0.015$ rad, $0.3 <$ p/E0 < 2, nSMDE > 1 and nSMDP > 1. On the Figure 4.11 the EMC efficiency as a function of p_T is plotted. Due to lack of statistics at high-p$_T$ I only studied the efficiency at p_T region from 1.2 to 4 GeV/c^2. At these intermediate p_T values the EMC efficiency is low and increases towards higher p_T.

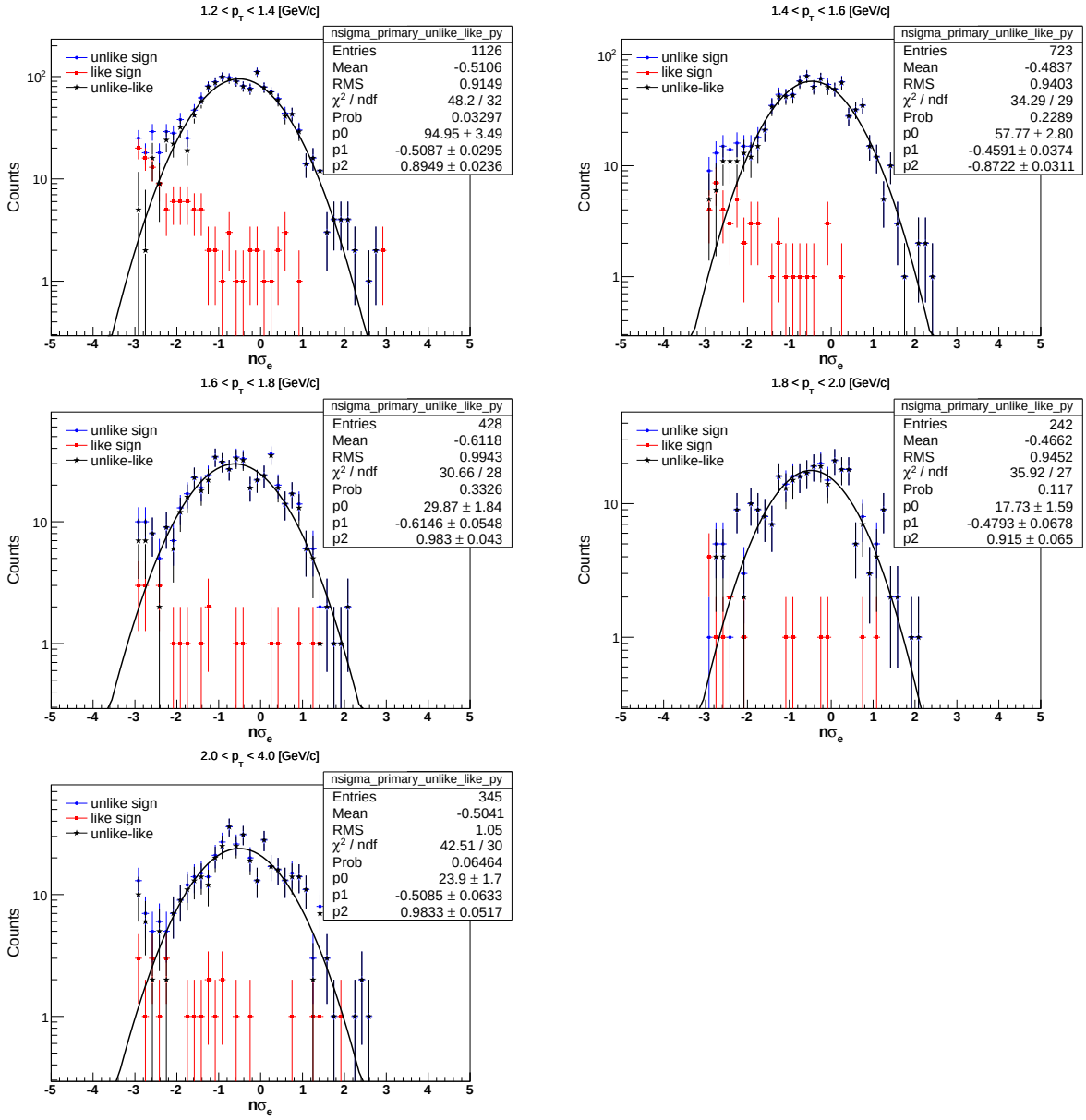

Figure 4.8: Distribution of $n\sigma_e$ of primary electron track of photonic electron pairs for unlike sign (blue dots), like sign electron pairs (red dots) and the unlike-like sign paris (black stars) for different p_T bins.

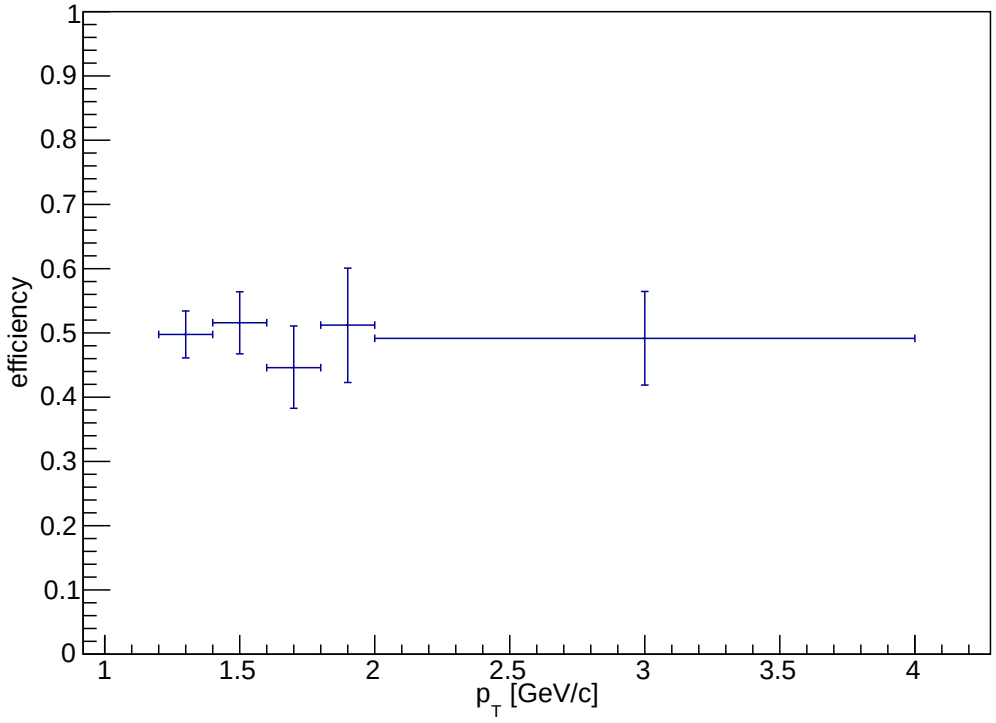

Figure 4.9: $n\sigma_e$ efficiency as a function of p_T.

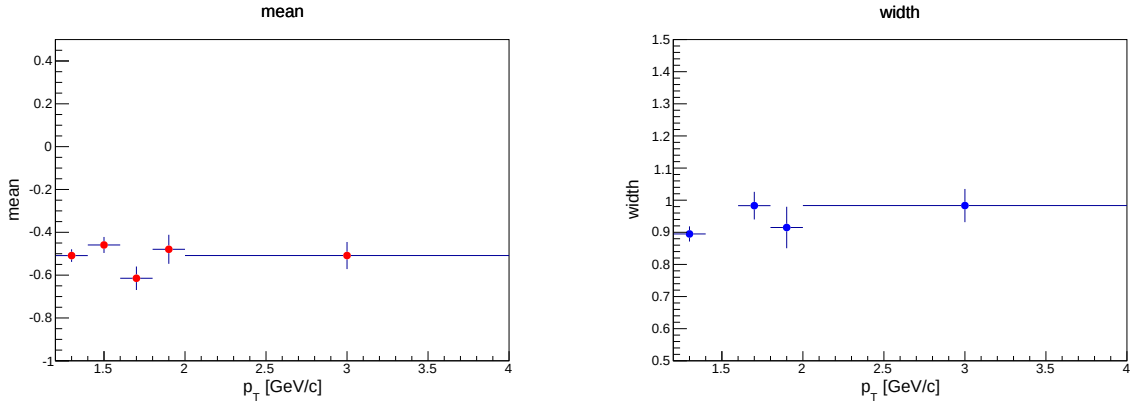

Figure 4.10: Distribution of mean and width of $n\sigma_e$ of primary electron track of photonic electron pairs obtained from the Gaussian fit.

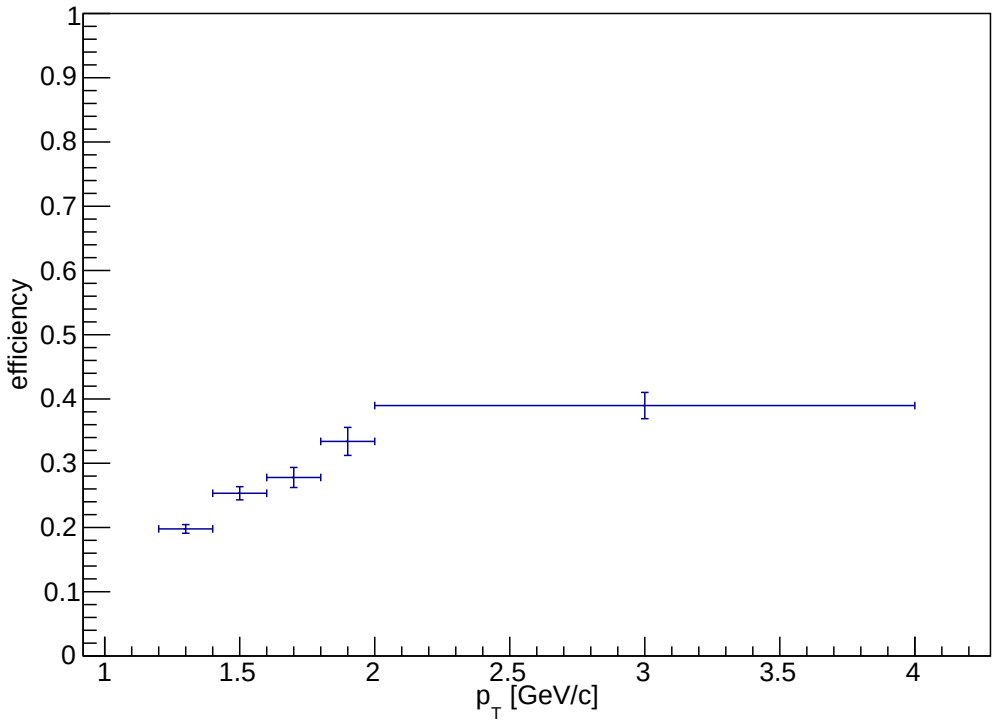

Figure 4.11: EMC efficiency as a function of p_T.

Conclusions

The aim of this work was to present in details the analysis of non-photonic electrons in UU collisions at energy $\sqrt{s_{NN}} = 193$ GeV in STAR experiment.

I presented here the purpose of heavy-flavor physics program, observables that help us understand what is going on during the earliest stages of heavy-ion collisions. I explained the reason why non-photonic electrons analysis is performed and in the last chapter I presented in detail steps of my analysis of non-photonic electrons in UU collisions at energy $\sqrt{s_{NN}} = 193$ GeV.

The work that have been performed on the study of non-photonic electrons is the following. The data sample in form of picoDst was obtained. Second, inclusive electron sample using event, track cuts and the electron identification cuts was selected. The way how these cuts were determined was explained and eventually it was verified that with the used cuts the pure electron sample is obtained. In the last section of the last chapter the calculation of cuts efficiencies was described. The efficiency of the $n\sigma_e$ cut is about 50 % and the efficiency of the EMC cuts starts at 20 % at $p_T = 1.2$ GeV/c and increases up to 40 % at $p_T \sim 4$ GeV/c.

Next step in my analysis will be the purity determination, that is the fraction of real electron tracks that are in my selected inclusive electron sample. In this work only a fraction of the data was presented. The same plots need to be obtained using entire data from UU collisions with central1 and central5 triggers. For subsequent analysis work it necessary to obtain the efficiency of the photonic electrons reconstruction via simulation that is called embedding. Finally the NPE yield has to be corrected on contributions from other particles.

Bibliography

[1] J. Beringer et al. (Particle Data Group), *Review of Particle Physics*, Phys. Rev. **D 86**, 010001 (2012).

[2] PHENIX Collaboration, *Enhanced production of direct photons in Au-Au collisions at* $\sqrt{s_{NN}} = 200$ *GeV and implications for the initial temerature*, Phys.Rev.Lett. **104**, 132301 (2010).

[3] R. Vogt, *Ultrarelativistic Heavy-Ion Collisions*, Elsevier 2007.

[4] R. Stock, *Relativistic Nucleus-Nucleus Collisions and the QCD Matter Phase Diagram*, arXiv: 0807.1610v1 (2008).

[5] Digal et al., *Quarkonium Feed-Down and Sequential Suppression*, Phys.Rev. **D64** 094015 (2001).

[6] M. Kliemant, R. Sahoo, T. Schuster and R. Stock, *Global Properties of Nucleus-Nucleus Collisions*, Lect.Notes Phys,. **785**, p. 23-103 (2010).

[7] Ch. Nattrass, *The Quark Gluon Plasma*, www.quantumdiaries.org.

[8] D. Cebra, *What we have learned from the RHIC Beam Energy Scan*, prezentĂ˘cia na APS California Section Meeting, San Luis Obispo CA, november 2012.

[9] K. Yagi et al., *Quark-Gluon Plasma*, Cambridge University Press 2005.

[10] J. Adams et al., *Centrality Dependence of Charged-Hadron Transverse-Momentum Spectra in d+Au Collisions at* $\sqrt{s_{NN}} = 200$ *GeV*, Phys. Rev. Lett. **91**, 072302 (2003).

[11] R. Field, *Min-Bias and the Underlying Event at the LHC*, arXiv: 1202.0901v1 (2012).

[12] David, *A smorgasboard of major experiment results*, www.ellipsix.net.

[13] Y.L. Dokshitzer and D.E. Kharzeev, *Heavy quark colorimetry of QCD matter*, Phys. Lett. **519**, 199 (2001).

[14] CMS Collaboration, *Suppression of non-prompt* J/ψ*, prompt* J/ψ *and* Υ*(1S) in PbPb collisions at* $\sqrt{s_{NN}} = 2,76$ *TeV*, arXiv: 1201.5069v1 (2012).

[15] The CMS Collaboration, *Observation of sequential Upsilon suppression in PbPb collisions*, Phys.Rev.Lett. **109**, 222301 (2012).

[16] The ALICE Collaboration, *Suppression of high transverse momentum D mesons in central PbPb collisions at* $\sqrt{s_{NN}} = 2.76$ *TeV*, JHEP 09(2012) 112.

[17] D. Tlustý, *Open charm hadron production via hadronic decays at STAR*, arXiv: 1211.5995v1 (2012).

[18] K. Kajimoto, *A Large Area Time of Flight Detector for the STAR Experiment at RHIC*, Ph.D thesis; U. of Texas at Austin (2009).

[19] P. Steinberg, *The Fight for RHIC*, www.quantumdiaries.org.

[20] Brookhaven National Laboratory, www.star.bnl.gov [online] [cit. 8.3.2014]

[21] S. Baumgart, *A Study of Open Charm Production in Heavy Ion Collisions of Center-of-Mass Energy 200 GeV per Nucleon*, Ph.D. thesis; Yale University (2009).

[22] The STAR Time Projection Chamber: A Unique Tool for Studying High Multiplicity Eventsat RHIC $http://www.star.bnl.gov/public/tpc/NimPapers/tpc/tpc\_nim.pdf$

[23] W. R. Leo, *Techniques for Nuclear and Particle Physics Experiments: A How-To Approach*, Springer, 1994.

[24] Proposal for a Large Area Time of Flight System for STAR, $http://www.star.bnl.gov/\ ruanlj/MTDreview2010/TOF_20040524.pdf$.

[25] The STAR Barrel Electromagnetic Calorimeter, $http://www.star.bnl.gov/public/-tpc/NimPapers/emc/emc\_nim.pdf$

[26] A Heavy Flavor Tracker for STAR, $http://rnc.lbl.gov/\ jhthomas/public/HeavyFlavor-Tracker/hft-06-08-2006.pdf$

[27] Proposal of a Midrapidity Dimuon Program at STAR: A Novel and Compact Muon Telescope Detector, $http://www.star.bnl.gov/\ ruanlj/MTDreview2010/-MTD\_proposal\_v14.pdf$

[28] STAR Collaboration, *High p_T non-photonic electron production in p+p collisions at $\sqrt{s} = 200$ GeV*, Phys.Rev. **D83**, 052006 (2011).

[29] M. Cacciari, P. Nason and R. Vogt, *QCD Prediction for Charm and Bottom Quark Production at RHIC* Phys. Rev. Lett. **95**, 122001 (2005).

[30] A. Knospe, *Charm production at RHIC*, ECONF C070805:10 (2007).

[31] M. M. Aggarwal et al. [STAR Collaboration], *Measurement of the Bottom Quark Contribution to Nonphotonic Electron Production in p+p Collisions at $\sqrt{s} = 200$ GeV* Phys. Rev. Lett. **105**, 202301 (2010).

[32] A. Knospe, *Yield and suppression of electrons from open heavy-flavor decays in heavy-ion collisions*, Ph.D. thesis; Yale University (2011).

[33] M. Mustafa for STAR Collaboration, *Measurements of Non-photonic Electron Production and Azimuthal Anisotropy in $\sqrt{s_{NN}} = 39, 62.4$ and 200 GeV Au+Au Collisions from STAR at RHIC*, arXiv: 1210.5199v2 (2012).

[34] B. I. Abelev for STAR Collaboration, *Erratum: Transverse momentum and centrality dependence of high p_T non-photonic electron suppression in Au+Au collisions at $\sqrt{s}_{NN} = 200$ GeV*, Phys.Rev.Lett. **98** 192301 (2007); Erratum-ibid. **106** 159902 (2011).

[35] B. Li, *Uranium on uranium collisions at relativistic energies*, Phys.Rev. **C61**, 021903 (2000).